Applied Energy 376 (2024) 124307

Contents lists available at ScienceDirect

Applied Energy

journal homepage: www.elsevier.com/locate/apenergy

Optimizing hydrogen spark-ignition engine performance and pollutants by combining VVT and EGR strategies through numerical simulation

Ricardo Novella, Josep Gomez-Soriano, David González-Domínguez *, Orlando Olaciregui

CMT–Clean Mobility & Thermofluids, Universitat Politècnica de València, Spain

HIGHLIGHTS

- Adaptation of a Euro 6 turbocharged DI SI engine for hydrogen operation
- Deep analysis of the VVT and EGR impact on thermal efficiency and emissions
- EGR dilution is more effective in reducing NO_X but penalizes fuel consumption
- EGR leads to a low-end torque increase of 5–16% at iso-NO_X conditions

ARTICLE INFO

Keywords:
Hydrogen combustion
Spark-ignition engine
Decarbonization
1D simulation
Exhaust gas recirculation

ABSTRACT

Hydrogen combustion engines are considered one of the leading solutions for decarbonizing road transport, mainly due to the possibility of adapting current engines for hydrogen operation with minor changes. This research extensively analyzes the effect of combined EGR (exhaust gas recirculation) and VVT (variable valve timing) strategies on the performance and emissions of a commercial turbocharged SI engine fueled with hydrogen. To this end, a 1D model of the said engine, widely validated for gasoline operation, was adapted to simulate the engine's behavior with hydrogen. This adaptation involved hardware changes and the implementation of a predictive hydrogen combustion submodel, previously calibrated using experimental data from a single-cylinder engine of similar geometry. Firstly, 400 hydrogen engine simulations without EGR were conducted to optimize the VVT system for fuel efficiency over a wide operating range. A detailed explanation of the causality of varying valve overlap on pumping losses, in-cylinder gas composition, and combustion is provided from these simulations. Then, a series of EGR sweeps were simulated to study its impact on performance and NOx at various degrees of load; concluding that diluting with EGR, rather than air, leads to reduced NOx emissions in exchange for slightly increased fuel consumption.

1. Introduction

Road transport contributes to 12% of global greenhouse gas emissions [1] and is the largest source of nitrogen oxide (NO_X) emissions [2]. In light of this, numerous governments are updating their standards to promote the sale of new on-road vehicles to reduce their environmental impact. The new criteria include decreasing the permissible levels of tailpipe emissions, utilizing more realistic vehicle homologation procedures, and even banning the use of fossil fuels in the future [3,4]. An example of this is the new legislation approved by the European Commission in 2023, which advocates for the complete decarbonization of cars and vans from 2035 [5]. In order to adapt to this challenging scenario, almost all manufacturers of light-duty vehicles are currently opting for powertrain electrification and alternative fuels.

Among the alternative fuels, a lot of research on powering internal combustion engines (ICEs) with hydrogen (H_2) is being done [6,7], given that H_2 is a carbon-free fuel whose unique combustion properties enable a conventional ICE to operate with high thermal efficiencies [8,9]. Welch et al. [10] supported this claim by conducting tests on a 0.5 L direct-injection single-cylinder engine, demonstrating that hydrogen-fueled ICEs can achieve brake thermal efficiencies of up to 45%. The main advantages of H_2 as a fuel are stated below. Firstly, hydrogen flames propagate extremely fast, shortening combustion duration and, accordingly, improving isochoric efficiency [11]. The high flame speeds of H_2 also lead to a much wider flammability range compared to other

* Corresponding author at: CMT–Clean Mobility & Thermofluids. Universitat Politècnica de València. Camino de Vera s/n, 46,022, Valencia, Spain.
E-mail address: dagondo1@mot.upv.es (D. González-Domínguez).

https://doi.org/10.1016/j.apenergy.2024.124307
Received 23 March 2024; Received in revised form 18 July 2024; Accepted 19 August 2024
Available online 31 August 2024

Nomenclature

Acronyms

AMF	air mass flow
BMEP	brake mean effective pressure
CAD	crank-angle degrees
DI	direct injection
DR	dilution rate
EGR	exhaust gas recirculation
EVC	exhaust valve closing
GPF	gasoline particulate filter
H_2	molecular hydrogen
HICE	hydrogen internal combustion engine
ICE	internal combustion engine
IMEP	indicated mean effective pressure
IVC	intake valve closing
IVO	intake valve opening
MFR	mass flow rate
NO_X	nitrogen oxides
PFI	port fuel injection
RGF	residual gas fraction
SI	spark ignition
SM	surge margin
TR	trapping ratio
TWC	three-way catalyst
VGT	variable geometry turbine
VVT	variable valve timing

Symbols

T	gas temperature
η	thermal efficiency
λ	air-to-fuel equivalence ratio

Subscripts

cyl	cylinder
ind	(net) indicated

fuels, like gasoline. Hydrogen-air mixtures can generally ignite if the air-to-fuel equivalence ratio (λ) is between 0.14 and 10, while gasoline-air mixtures are only flammable for λ values from 0.26 to 1.51 [12].

Therefore, hydrogen internal combustion engines (HICEs) can operate at ultra-lean conditions, avoiding throttling at partial loads and lowering heat losses [13]. High dilution operation, through either air or exhaust gases, also reduces the production of NO_X, the only pollutants potentially generated during H_2 combustion [14,15]. In addition, compared to stoichiometric gasoline-air ones, lean hydrogen-air mixtures have higher specific heat ratios and even allow for larger compression ratios, both increasing the theoretical thermal efficiency of the engine cycle [16,17]. Oh et al. [18] provided evidence of this by reporting that the considerable knocking resistance of H_2, derived from its high autoignition temperature, enabled the compression ratio to be enlarged to 17 in a heavy-duty single-cylinder engine.

However, the use of hydrogen in ICEs is not exempt from issues. Its combustion properties make hydrogen desirable but can bring about abnormal combustion phenomena, such as knocking, preignition (i.e. due to surface ignition) and backfiring [11]. It should be noted that the minimum energy required to ignite hydrogen-air mixtures is around 12 times lower than for gasoline-air mixtures [19], predisposing HICEs to preignition events. Preignition usually arises from surface ignition at hot spots in the combustion chamber [13]. When this phenomenon occurs during the intake stroke in a port fuel injection (PFI) engine, the flame may propagate out of the cylinder, burning the hydrogen in the intake manifold, thus giving rise to a backfire event [20]. Another relevant drawback of hydrogen is its low density, complicating fuel storage and, potentially, comprising the driving range. Besides, its low density, along with its elevated stoichiometric air-to-fuel ratio, can lead to a power output loss in PFI engines [6], owing to the significant portion of the intake manifold volume occupied by the hydrogen. Direct injection is the best option to mitigate such a power loss and avoid backfiring [21].

Despite these issues, many experts assert that HICEs will play a key role in the transportation sector in the following decades [22,23], largely thanks to the feasibility of converting existing engine systems for hydrogen operation with minor changes. This research is, therefore, devoted to studying the performance and emissions of a Euro 6 turbocharged direct-injection (DI) spark-ignition (SI) engine adapted to be fueled with hydrogen, keeping the DI system. The said engine is equipped with advanced technologies, such as exhaust gas recirculation (EGR), variable valve timing (VVT), and variable geometry turbine (VGT), adding complexity to the process of optimizing its performance due to the multiple degrees of freedom. There is a common understanding that simulation tools are the most effective way to address that kind of process, at least from the cost and time perspective.

In the present work, a 1D model of the whole SI engine under consideration is employed, including all the technologies mentioned above. The model, previously calibrated through experimental tests using gasoline as fuel, is adapted to simulate engine operation with hydrogen. This adaptation mostly involves hardware changes to preserve the original peak power and a dedicated H_2 combustion model. Then, spark timing, EGR rate, and VVT settings are optimized via simulation over a wide operating range for fuel economy, considering knocking and NO_X emissions as well. To the best of the authors' knowledge, no published studies have addressed the performance optimization of a multi-cylinder hydrogen-fueled engine from such a holistic perspective, including the interactions between advanced technologies like DI, VGT, VVT and EGR. Therefore, the main contribution of this research is providing a deep analysis of how EGR and VVT strategies affect the thermal efficiency, power output, and emissions of a commercial SI engine fueled with hydrogen, offering valuable insights for optimizing HICE and implementing them in transportation.

The paper is structured as stated below. Section 2 details the numerical simulation tool, describing the engine, the 1D model and its calibration, and the predictive hydrogen combustion submodel. Section 3 is devoted to the methodology followed, and Section 4 presents the simulation results and discussion. Finally, the main conclusions are given in Section 5.

2. Engine model

2.1. The base engine

A four-cylinder downsized (1.3 l) turbocharged DI SI gasoline engine, originally equipped with EGR, VVT and VGT technologies, was selected for this research. The cooled low-pressure EGR system is composed of a T-shape flow splitter to extract the exhaust gases previously treated, a water-to-air intercooler, and two valves: one in the EGR loop itself, just downstream of the said intercooler; and the other placed in the intake line, upstream of the EGR joint, to increase the pressure difference between intake and exhaust sides if needed. Utilizing the VVT system, the intake and exhaust valve timings can be independently shifted within a range of 40 crank-angle degrees (CAD), without altering the valve lift or opening duration. Besides, the VGT turbocharger enables a maximum boost pressure of 2.5 bar. Table 1 provides the main engine's specifications [24].

Moreover, this engine incorporates a compact water charge air cooler (WCAC) integrated into the intake manifold and a Euro 6 after-

Table 1
Engine's attributes [24].

Attribute	Description
Technology	Euro 6 turbocharged DI SI gasoline
Displacement	1300 cc
Bore / Stroke	72.20 / 81.35 mm
Compression ratio	10:1
Number of cylinders	4
Camshaft system	VVT
Total number of valves (intake/exhaust)	8/8
Turbocharger	Water-cooled with VGT
Aftertreatment system	TWC + GPF

treatment system, which consists of a conventional three-way catalyst (TWC) and a gasoline particulate filter (GPF). Fig. 1 depicts the schematic engine's layout [24], including all the systems and technologies mentioned.

2.2. Model description

A 1D model of the SI engine presented in the former section was built with GT-POWER software, including all the components shown in Fig. 1. Pressure losses are computed using the Fanning factor, considering surface roughness and Reynolds number; and the convective heat transfer is estimated using the Colburn analogy in ducts and volumes and the classic Woschni correlation in the cylinders. The turbocharger submodel is fed with extrapolated and adiabatized compressor and turbine maps, measured under hot-exposed conditions by the manufacturer. The method of extrapolating and adiabatizing these maps is given in [25]. The following data provided by the engine manufacturer is also used: valve characteristic curves, intake and exhaust valve lift profiles, and thermal efficiencies of the WCAC and EGR cooler.

This engine model, already utilized in two previous studies [24,26], was calibrated according to the procedure defined in [27] to enable accurate and predictive simulations. Empirical correlations and an artificial neural network (ANN) were integrated into the model to adjust heat transfer and pressure drop phenomena and to predict standard Wiebe function parameters for gasoline combustion [28]. A general overview of the calibration procedure is given in Section 2.3. Finally, to predict the engine performance with hydrogen, the standard Wiebe function is substituted with a dedicated H_2 combustion model, calibrated using experimental data from tests conducted on a single-cylinder ICE with similar geometry detailed in [15]. A description of the predictive hydrogen combustion submodel is provided in Section 2.4.

2.3. Model calibration

The 1D model was calibrated with data from gasoline-fueled engine tests. To this end, the SI engine presented in Section 2.1 was installed and fully instrumented on a dynamic test bench to regulate its operation and acquire all desired data, such as torque and speed, pressure and temperature values in relevant parts, mass flows, exhaust emissions, and in-cylinder pressure signals. The location of some sensors and measurement devices can be observed in Fig. 1. A detailed description of the test bench and instrumentation is given in former works [24,26].

About 300 steady-state tests were carried out by varying EGR rate and VVT settings for 16 operating points, particularly selected to cover most of the engine operation during a WLTP driving cycle [24]. More specifically, 18 cases per operating point were tested by combining six EGR rates (0–25%) with three pairs of VVT settings (minimum, intermediate, and maximum valve overlaps). Besides, in each test, the spark timing was adjusted in real time to achieve a CA50 (the crank angle at which 50% of the heat is released) value between 5 and 10 CAD after top dead center [29], provided that knocking was avoided.

Model calibration involved three stages: tuning of fitting parameters, model validation, and obtention of empirical correlations [24]. Firstly, the 300 tests were reproduced with the 1D model to adjust pressure drop and convection multipliers (fitting parameters). Tuning the fitting parameters was automated with (PI) proportional-integral controllers, targeting the actual cycle-averaged temperature and pressure values at the intake and exhaust manifolds and around the turbocharger. In addition, for these simulations, the turbocharger was decoupled to

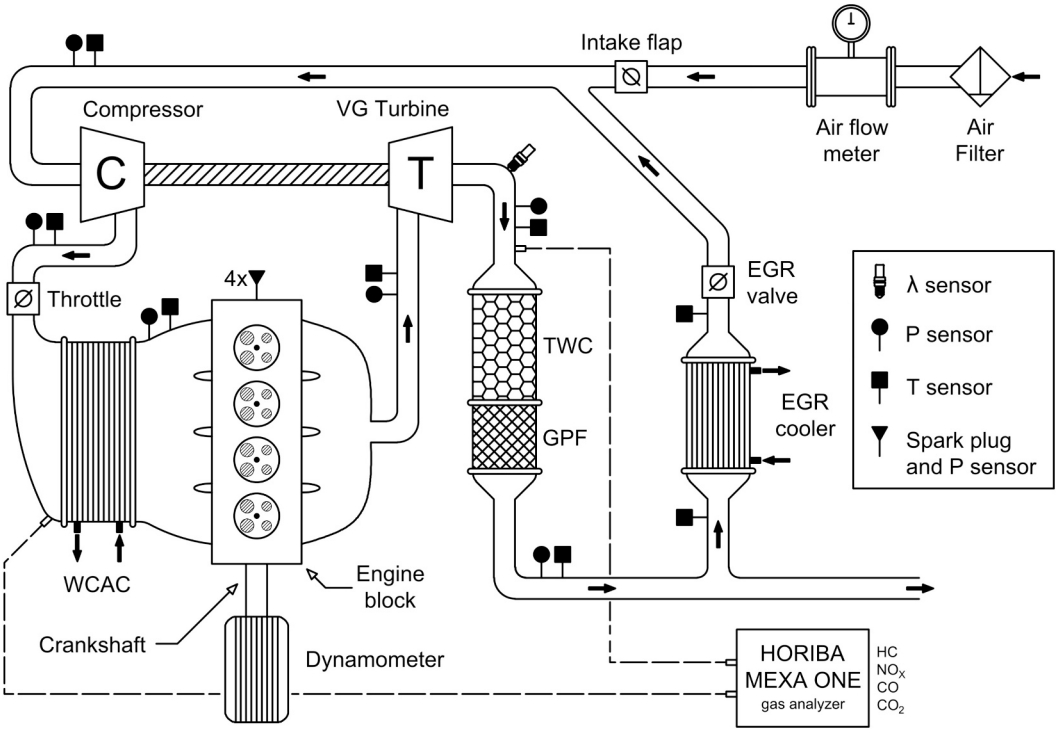

Fig. 1. Schematic layout of the engine with instrumentation [24].

simultaneously regulate the intake and exhaust manifold pressures [27].

In the second stage, the results from the 300 engine simulations were validated. The experimental and predicted values of air mass flow (AMF) and indicated mean effective pressure (IMEP) were compared, and the instantaneous pressure traces in the cylinders and manifolds were checked. An error threshold of 5% was considered for AMF and IMEP variables, so only the fitting parameters from simulations with these errors below 5% were employed as inputs for empirical correlations [24,26]. Fig. 2 presents AMF (a) and IMEP (b) errors related to modeling the 300 engine tests previously mentioned [24]. Two types of errors are provided for each variable per operating point: the mean absolute percentage error (MAPE) and maximum error (in absolute valve). These plots show that errors in AMF and IMEP do not exceed the 5% threshold.

Thirdly, empirical correlations were obtained with the validated fitting parameters, and an ANN was trained using experimental and predicted data, as explained in [27], to predict Wiebe equation parameters. Table 2 shows the following attributes of the correlations and ANN incorporated into the 1D model of the gasoline engine: (i) the involved variable; (ii) the fitting parameter or correlation output; (iii) the independent variables; (iv) the type of correlation; and (v) the coefficient of determination [27]. Finally, the model calibration was finished by implementing the correlations and ANN, recoupling the turbocharger, and removing all PI controllers, except the one that adjusts engine load. After that, the engine model was ready to run predictive simulations.

2.4. Predictive H_2 combustion submodel

The abovementioned ANN, trained to predict gasoline combustion, is clearly unusable for this research. The predictive H_2 combustion submodel used instead is described below. Hydrogen combustion simulation is conceptualized as a spark-ignited model; specifically, the Coherent Flame Model (CFM) combustion model [30,31] is selected. This model incorporates the interplay between turbulence and combustion phenomena. Turbulence levels are numerically characterized using detailed 3D CFD simulations including intake, exhaust and combustion chamber components. The model integrates turbulent flow with flame reactions, as represented by **Eq. (1)** that calculates the burning rate ($\dot{m}_b$), where ρ_{ub} denotes unburnt gas density, and A_f signifies effective flame area accounting for turbulence-induced wrinkling.

$$\dot{m}_b = \rho_{ub} \cdot A_f \cdot S_L \tag{1}$$

$$A_f = A_{geo} \cdot \Phi \cdot f_{wall} \tag{2}$$

The impact of turbulence on flame propagation rate is quantified through Eq. (2), which models a spherically propagating flame with geometrical area (A_{geo}) defined by its radius and incorporates a term (Φ) addressing the effect of turbulence on flame speed. Furthermore, an additional term (f_{wall}) is introduced to accommodate flame front deactivation upon interaction with combustion chamber walls. Comprehensive details regarding the fundamental principles of this combustion model are available in [32].

The component of the effective burning rate reliant on fuel chemistry and its reaction properties is introduced through the laminar flame speed (S_L). In this study, S_L is integrated into the model by means of an ANN, which captures the non-linear trends inherent in thermo-chemical oxidation properties. The ANN was trained using a validated database of laminar flame speed simulations derived from the Chemical Reaction Engineering and Chemical Kinetics Lab [33]. The training of the ANN encompassed a wide simulation matrix spanning pressures from 1 to 190 bar, temperatures from 600 to 1800 K, and equivalent air-to-fuel ratios from 1.05 to 4, including EGR rates of up to 40%.

In order to address the objectives of the present study, the simulation environment also incorporates an extended Zeldovich mechanism [34] to estimate NO_X emissions. Considering that a significant portion of NO_X emissions from HICE combustion is reported to be NO [35], the included reactions solely focus on NO formation (**Eqs. (3)-(5)**). The reaction rates are calculated using the Arrhenius expression, with the activation energy and Arrhenius factor as calibration parameters for each chemical transformation.

$$O + N_2 \rightarrow NO + N \tag{3}$$

$$N + O_2 \rightarrow NO + O \tag{4}$$

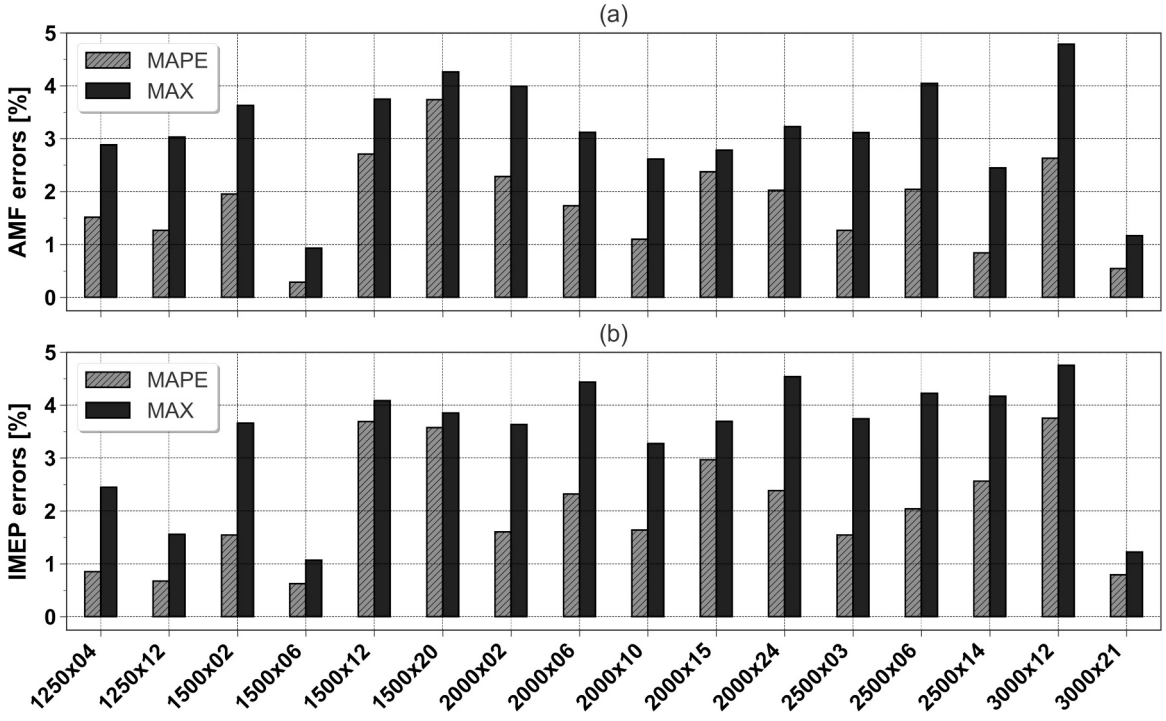

Fig. 2. Modeling errors in AMF (a) and IMEP (b) related to the 16 working points used for the model calibration. In the x-axis labels, the first value is engine speed (rpm) and the second is engine BMEP (bar) [24].

Table 2
Attributes of the empirical correlations and ANN implemented into the 1D model of the gasoline engine [24]. (*) R^2 related to the ANN training data set.

Involved variable	Fitting parameter	Independent variables	Correlation type	R^2
Compressor inlet pressure	FM of the air filter	Air volume flow	Quadratic polynomial equation	0.98
Intake manifold temperature	WCAC coolant flow	Engine speed and IMEP	3D map from scattered data	–
Turbine inlet temperature	HTM of the exhaust manifold	Gas temperature at the exhaust ports and gas mass flow through the turbine	Linear polynomial equation	0.81
Turbine outlet pressure	FM of the TWC and GPF	Gas volume flow at the GPF inlet	Quadratic polynomial equation	0.97
GPF outlet pressure	FM of the exhaust line	Gas volume flow through the exhaust line	Quadratic polynomial equation	0.98
EGR cooler inlet temperature	HTM of the EGR line	Gas temperature at the GPF outlet and EGR mass flow	Linear polynomial equation	0.75
EGR cooler outlet temperature	Coolant flow in the EGR cooler	Engine speed and IMEP	3D map from scattered data	–
Combustion phasing (Wiebe function)	CA50	Spark timing, AFR, engine speed and in-cylinder pressure, temperature, trapped mass and residual gas fraction at IVC.	Quadratic polynomial neural network	0.98*
Combustion duration (Wiebe function)	CA1090	Spark timing, AFR, engine speed and in-cylinder pressure, temperature, trapped mass and residual gas fraction at IVC.	Quadratic polynomial neural network	0.96*
Engine friction losses	FMEP	Engine speed and maximum cylinder pressure	Chen-Flynn model	0.81

HTM: heat transfer multiplier; FM: friction multiplier; IVC: intake valve closing.

$$N + OH \rightarrow NO + H \quad (5)$$

The hydrogen combustion model, including the NO_X submodel, was calibrated and validated in a former study [15] using data from tests and 1D simulations on a single-cylinder hydrogen-fueled SI research engine. This engine is essentially a single-cylinder version of the original engine, with only minor modifications to the stroke and bore lengths. All other parameters related to the combustion system, including the chamber and ports design, injector, and ignition system, remain identical in both engines. Therefore, it is reasonable to expect that the thermodynamic properties of the flow will remain fairly similar in both cases. Regarding the calibration, seven experiments were replicated with the 1D model of the single-cylinder engine to calibrate ten multipliers: four for the wrinkling term (Φ) in Eq. (2) and six others for scaling the activation energies and Arrhenius factors of NO formation reactions. Fourteen additional tests were simulated for validation, confirming that the combustion model predicts both heat release rate and NOx emissions with tolerable errors [15].

Additionally, a semi-empirical submodel is utilized to assess abnormal knocking combustion. This submodel lies in the classical correlation by Douaud and Eyzat [36], which estimates the induction time as a function of the octane number, the in-cylinder pressure and temperature at spark timing, and some calibration coefficients adjusted with experimental data. The dilution effect is considered through one of these coefficients. This way, despite its simplicity, the submodel is capable of qualitatively capturing the knock trend as the dilution, combustion phasing, and compression ratio are varied [15].

3. Methodology

The main objective of the present work is to study the impact of EGR and VVT strategies on the overall performance and emissions of a commercial automotive SI engine fueled with hydrogen. To this end, firstly, some changes were introduced into the 1D model to adapt the engine for hydrogen operation, and then, the VVT settings and EGR rate were sequentially optimized for the 16 steady-state operating conditions presented in Section 2.3. Despite its limitations in computational efficiency and global optimality, this simple optimization method based on sequential one-variable sweeps facilitates analyzing the effects of VVT and EGR strategies on thermal efficiency and NO_X emission. The whole methodology followed is detailed below.

The goal of the engine adaptation was to preserve the original SI engine performance using hydrogen as a fuel with λ equal to 2. This λ value ensures low NO_X levels and reduced knocking risk [37,38]. Regarding the changes in the 1D model, the exhaust line diameter was enlarged by 20% to minimize pressure losses, and the exhaust manifold was insulated with a rock-wool layer of 50 mm to reach higher temperatures at the turbine inlet. The gasoline TWC and GPF devices were maintained to partially replicate pressure drop phenomena in hydrogen aftertreatment systems, which would potentially consist of a selective catalytic reduction device, an ammonia slip catalyst, and even a particulate filter to eliminate particulate matter resulting from lubricating oil combustion [39]. In addition, the turbocharger was scaled to increase turbine expansion ratio and avoid compressor surge. A reduction of 10 and another of 20% in turbocharger size were tried by decreasing the mass flow rate data of turbine and compressor maps accordingly.

Ten engine simulations were run to determine which option was the most suitable. In particular, the original full-load curve between 1250 and 3000 rpm was attempted to be replicated by applying the two reductions in turbocharger size, along with the other hardware changes mentioned above, and considering the thermo-mechanical limits listed in Table 3. In the interest of simplicity, a simple Wiebe function with constant parameters was utilized to reproduce combustion in these ten simulations.

After the 1D model adaptation, a series of parametric hydrogen engine simulations without EGR were performed to optimize VVT settings for each of the 16 operating conditions selected. Twenty-five pairs of IVO (intake valve opening) and EVC (exhaust valve closing) values per working point, a total of 400 cases, were simulated to find the best VVT configuration in terms of net indicated thermal efficiency (η_{ind}). For the 400 cases, the ambient pressure and temperature were set to 1 atm and 25 °C, the WCAC cooling capacity was regulated to keep the intake manifold at 30 °C, and a λ value of 2 was imposed. Besides, the predictive H_2 combustion submodel described in Section 2.4 was implemented, and the spark timing was adjusted using a specialized optimizer to maximize η_{ind} in each case.

Regarding the results of these simulations, the impact of the VVT strategy on pumping, heat and exhaust losses, combustion duration (CA1090), and residual gas fraction was assessed to understand its effect on η_{ind}. The residual gas fraction (RGF) is calculated as the ratio between the mass of burned gases (including external EGR if applicable) trapped in the cylinders at IVC (intake valve closing) and the total mass trapped.

Table 3
Turbocharger and engine thermo-mechanical limits.

Variable	Maximum value
Turbocharger speed	250,000 rpm
Compressor outlet temperature	200 °C
Turbine inlet temperature	950 °C
Turbine inlet pressure	4.2 bar
In-cylinder pressure	180 bar

It should also be clarified that only the results from those simulations in which the VVT configuration provided a trapping ratio (TR) of 1 were analyzed. This way, those cases with an effective air dilution at the combustion chamber lower than 100% ($\lambda = 2$) were excluded to ensure a fair comparison. The trapping ratio is defined in **Eq. (6)**, where $m_{air,tp}$ is the mass of air (kg) trapped in the cylinders at IVC, ω_{eng} the engine speed (s^{-1}), and $\dot{m}_{air}$ the total mass flow rate of air (kg/s). The parameter "i" is equal to 0.5 for four-stroke engines.

$$TR\ (\%) = 100 \cdot \frac{m_{air,tp} \cdot \omega_{eng} \cdot i}{\dot{m}_{air}} \tag{6}$$

Lastly, parametric H_2 engine simulations with EGR were carried out to evaluate the benefits and drawbacks of this strategy. More specifically, a series of EGR sweeps were simulated under two different intake charge conditions:

- **Iso-dilution conditions**. A constant external (not including internal EGR) dilution rate of 100% is guaranteed in each simulation by replacing a portion of air with EGR gases. A dilution rate (DR) of 100% is the one achieved with $\lambda = 2$ without EGR. From the concepts of λ, EGR rate and dilution, presented in **Eq. (7), (8), and (9)**, it follows that reducing λ by 0.1 means increasing the EGR rate by 5% if keeping DR at 100%, as shown in **Eq. (10)**.

$$\lambda = \frac{\dot{m}_{air}}{\dot{m}_{air,st}} \tag{7}$$

$$EGR\ rate\ (\%) = 100 \cdot \frac{\dot{m}_{EGR}}{\dot{m}_{air} + \dot{m}_{EGR}} \tag{8}$$

$$DR\ (\%) = 100 \cdot \left(\frac{\dot{m}_{air} + \dot{m}_{EGR}}{\dot{m}_{air,st}} - 1 \right) \tag{9}$$

$$EGR\ rate\ (\%) = 100 - 50\lambda, \text{ if } DR = 100\% \tag{10}$$

The variable $\dot{m}_{air,st}$ refers to the stoichiometric mass flow of air for a given mass flow of fuel, while $\dot{m}_{EGR}$ is the mass flow of exhaust gases recirculated. One EGR sweep, from 0 to 25% EGR in increments of 5%, was simulated under iso-dilution conditions for each of the following four operating points: 1250 rpm and 4 bar BMEP (low engine load), 1500 rpm and 6 bar BMEP (medium-low), 2500 rpm and 14 bar BMEP (medium-high), and 2000 rpm and 24 bar BMEP (high). For every sweep, constant IVO and EVC values equal to the optimal ones (previously calculated for $\lambda = 2$ and no EGR) were used. The analysis of the results focused on explaining the effect on η_{ind} and NO_X emissions through variables such as combustion temperature and duration.

- **Iso-NO_X conditions**. EGR gases are more effective than fresh air in minimizing NO_X emissions [40], so the EGR strategy can lead to a higher low-end torque due to a reduced boost request (given that a lower DR is required for the same NO_X level). Hence, several engine simulations were conducted to determine maximum torque at 1250 and 1500 rpm for λ values between 1.1 and 2. For every λ value, the EGR rate was adjusted to maintain NO_X emissions (in g/h) at the same level as the one achieved with $\lambda = 2$ and no EGR.

For all simulations with EGR, the ambient pressure and temperature were set to 1 atm and 25 °C, and the cooling capacities of the WCAC and EGR cooler were adjusted to keep the intake manifold and the EGR cooler outlet at 30 and 90 °C, respectively. Likewise, the predictive H_2 combustion submodel and the spark timing optimizer were also used.

4. Results and discussion

4.1. Engine modification for hydrogen operation

Firstly, five engine simulations were performed to determine maximum torque at 1250, 1500, 2000, 2500 and 3000 rpm using hydrogen as a fuel, without any modifications regarding the original engine configuration. Fig. 3 illustrates the engine torque (a), normalized by the maximum torque with gasoline, and the corresponding opening of the VGT vanes (b) for the five simulations mentioned. These five cases with hydrogen are labeled as "baseline with H_2". The full-load curve with gasoline is also represented in **Fig. 3**a (solid line). This graph shows that the maximum torque between 1250 and 2000 rpm is clearly lower with hydrogen while VGT is fully closed. The most significant power loss is around 50% at 1500 rpm.

In order to compensate for the power loss, the exhaust system was altered, as described in Section 3, and two reductions of 10 and 20% in turbocharger size were tried. It should be remarked that, for each turbocharger size reduction, the mass flow rate (MFR) data of turbine and compressor maps were modified in the same proportion. Ten hydrogen engine simulations at full-load conditions were conducted to evaluate which of the two options is better: five cases (1250, 1500, 2000, 2500 and 3000 rpm) with a 10% reduction and the remaining five with 20%. Fig. 4 shows engine torque (a), VGT opening (b), turbine inlet temperature (c), and turbine expansion ratio (d) for these ten simulations, and for the five comparable cases in Fig. 3 simulated using the original engine configuration. The torque data in **Fig. 4**a are normalized by the maximum torque with gasoline. Fig. 5 depicts the compressor outlet temperature (a), surge margin (b), turbocharger speed (c), and maximum in-cylinder pressure (d) for the same cases as in Fig. 4. The surge margin (SM) is defined as the difference between the corrected MFR through the compressor and the theoretical corrected MFR at the surge line for a given pressure ratio, divided by the latter; so negative SM values entail that the compressor is surging.

Decreasing the turbine size allows for an increase in the expansion ratio for a defined VGT position, and insulating the exhaust manifold raises the temperature at the turbine inlet. Both modifications result in increased torque between 1250 and 2000 rpm compared to the baseline scenario. In particular, scaling the turbocharger down by 20% is the best option, given that the gasoline full-load torque at 1250 rpm cannot be replicated by applying a reduction of only 10% (**Fig. 4**a). In addition, reaching the original peak power at 1500 rpm with a 10% reduction would not be feasible either because the compressor would be surging (**Fig. 5**b). It proves that decreasing the compressor size by 20% is also required. Regarding the thermo-mechanical limitations, it should be stated that all the limit values defined in Table 3 are met, as noticed in Fig. 4 and Fig. 5.

4.2. VVT optimization

The results of the hydrogen engine simulations conducted to optimize IVO and EVC settings for all 16 selected operating points are presented in this section. Given that the influence of VVT on fuel efficiency remains consistent for certain degrees of load across different engine speeds, the results of this study can be classified into three categories: throttling, no-throttling (open throttle), and turbocharging conditions.

4.2.1. Throttling conditions

Fig. 6 illustrates the contour maps of pumping losses (a), in-cylinder RGF (b), combustion duration (c), and (net) indicated efficiency (d) as functions of IVO advance and EVC delay (in CAD) at 1250 rpm and 4 bar BMEP. These maps were obtained by interpolating the results from simulating twenty-five pairs of VVT settings at this working point under the conditions described in Section 3. All the contour maps presented in this research were determined by following the same method, regardless of either the variable or the operating point. Besides, it should be stated

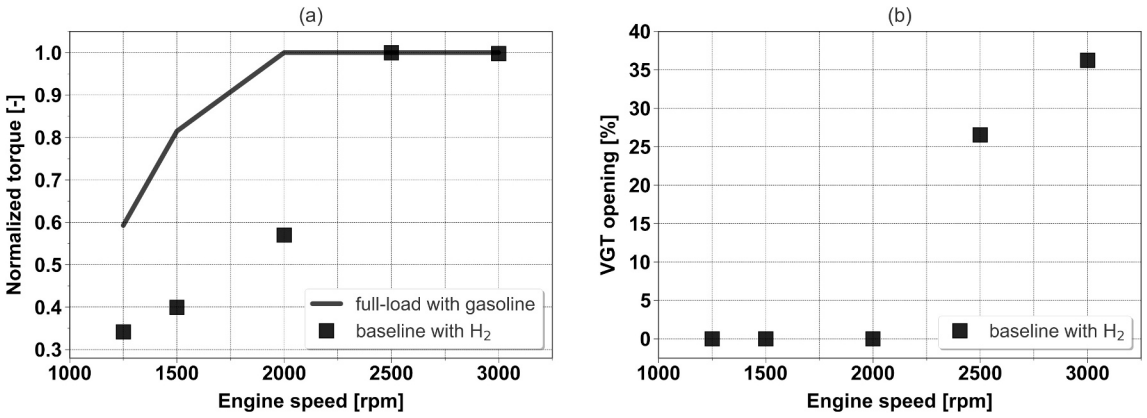

Fig. 3. Normalized engine torque (a) and VGT position (b) at full-load operation with hydrogen using the baseline engine configuration.

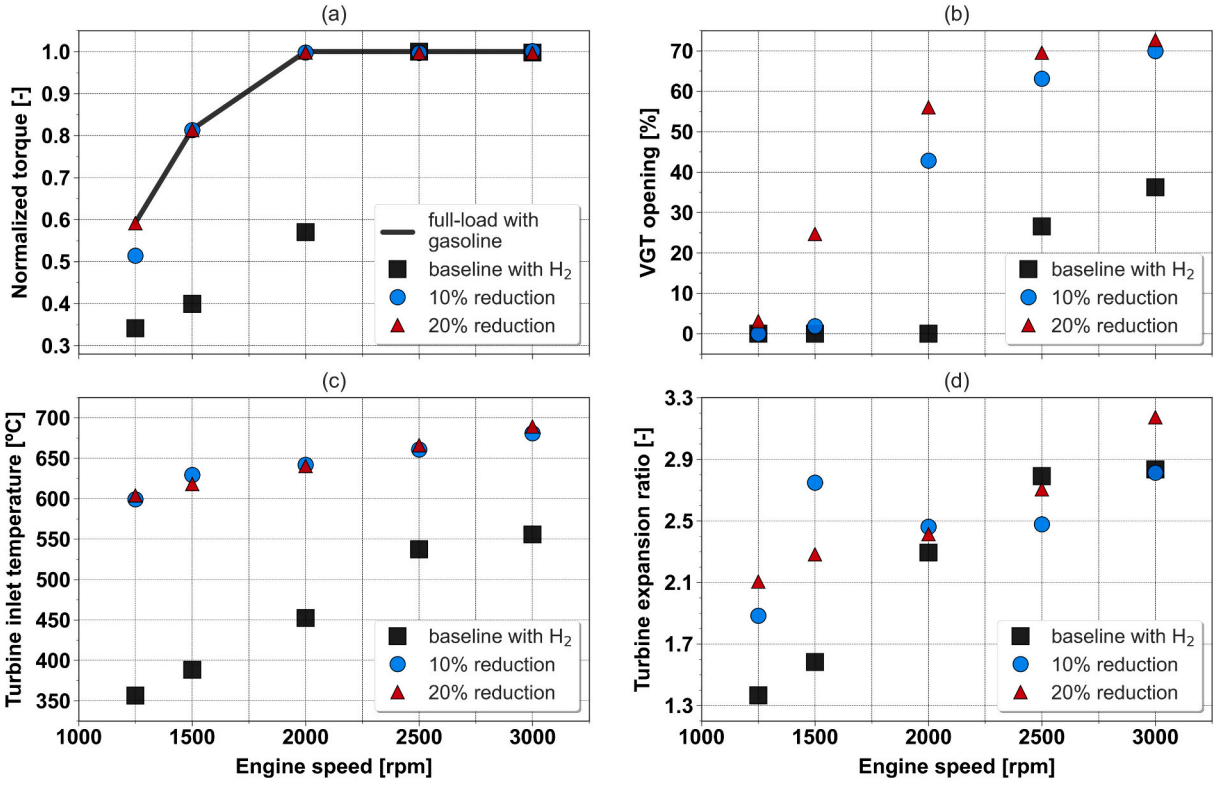

Fig. 4. Normalized engine torque (a), VGT position (b), turbine inlet temperature (c), and turbine expansion ratio (d) at full-load operation with hydrogen through 10 and 20% reduction in turbocharger size.

that IVO and EVC values equal to 0–0 and 40–40 provide the minimum and maximum valve overlaps, respectively. In order to fully understand the results, the best and worst cases in terms of efficiency, marked with a cross (VVT 40–30) and a circle (VVT 20–0) in Fig. 6d, are compared. Fig. 7 shows the instantaneous MFR through each intake valve (a) and in-cylinder temperature (b) for the two VVT configurations mentioned.

Increasing the valve overlap leads to higher in-cylinder RGF, causing a reduction in pumping losses. This is because lower throttling is required to increase valve MFR in the second half of the intake stroke, thus compensating for backflows during the valve overlap (around 360 CAD), as seen in Fig. 7a. It should be stated that, at this operating point, the cycle-averaged intake manifold pressure is between 0.6 and 0.9 bar (depending on VVT settings), while there is about 1.05 bar at the exhaust manifold. On the other hand, as RGF increases, the combustion process is slower, and heat losses are slightly larger despite a lower combustion temperature. The latter is due to the fact that more residual gases also lead to a higher in-cylinder temperature during the intake and compression strokes (Fig. 7b). These two adverse effects, particularly the longer combustion duration, explain why the indicated efficiency is optimized using the VVT 40–30 configuration rather than the one of maximum overlap (VVT 40–40), which minimizes pumping losses (Fig. 6a). The VVT strategy at 1250 rpm and 4 bar BMEP can improve indicated efficiency by up to 1.5% (Fig. 6d).

4.2.2. *Open throttle conditions*

Fig. 8 illustrates the contour maps of pumping losses (a), in-cylinder RGF (b), combustion duration (c), and (net) indicated efficiency (d) as functions of IVO advance and EVC delay at 1500 rpm and 6 bar BMEP. Under these engine running conditions, no throttling is practically required, and the VGT vanes are still kept fully open. Hence, the intake

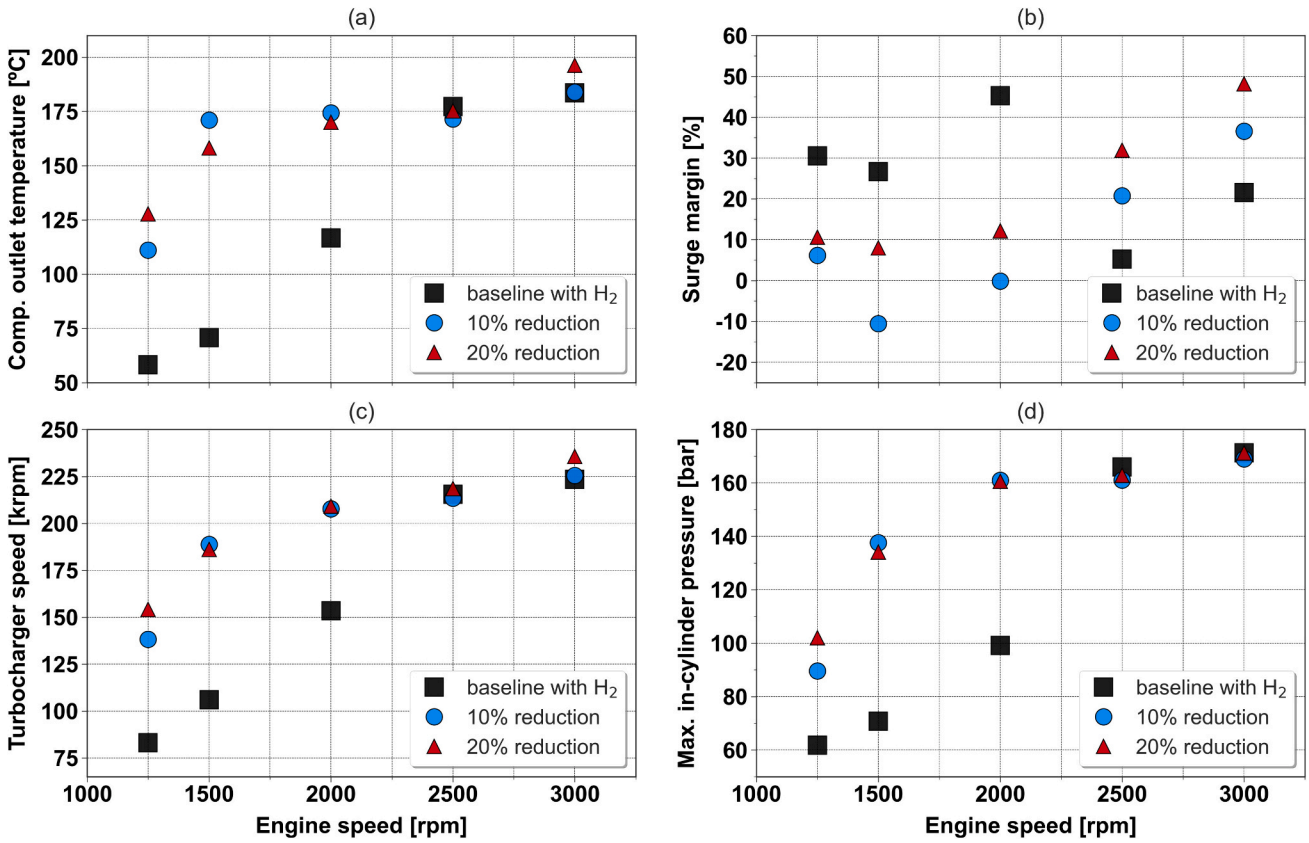

Fig. 5. Compressor outlet temperature (a), surge margin (b), turbocharger speed (c), and maximum in-cylinder pressure (d) at full-load operation with hydrogen through 10 and 20% reduction in turbocharger size.

manifold is nearly at the ambient pressure while the exhaust manifold is at 1.1 bar. The results obtained using the VVT 0–20 and VVT 40–20 configurations (respectively marked with a circle and cross in Fig. 8d) are compared to analyze the effect of advancing IVO and, thus, understand the differences in shape between the maps of pumping losses and indicated efficiency. Fig. 9 depicts the instantaneous MFR through each intake valve (a) and in-cylinder temperature (b) for the cases simulated with VVT 0–20 and VVT 40–20.

As the intake manifold pressure is closer to the exhaust one, the backflows through intake valves during the overlap period are smaller. As a consequence, the reduction in pumping losses that can be achieved with a longer valve overlap is increasingly less significant. Fig. 8a shows that pumping losses are reduced only by around 0.2% when advancing IVO by 40 CAD (for an EVC delay of 20 CAD). This minor effect is because the intake manifold pressure barely increases; given that the backflows during the overlap period through an IVO advance of 40 CAD are comparable to the ones obtained without advancing IVO at the beginning of the compression stroke (Miller cycle). In Fig. 9a, the valve overlap happens at around 360 CAD, and the compression stroke starts at 540 CAD.

Although the quantity of backflows is similar for both VVT configurations, their composition differs. Backflows are exclusively composed of burnt gases when occurring upon IVO (as with VVT 40–20), while they are mainly comprised of fresh air if taking place just before IVC (as with VVT 0–20). This distinction is responsible for an RGF increase of 4% when advancing IVO by 40 CAD, leading to a bit worse combustion (Fig. 8c). Regarding heat losses, the effect of varying IVO is very marginal. Fig. 9b shows minor in-cylinder temperature differences between the two VVT configurations mentioned, with slightly lower temperatures during combustion and slightly higher ones during the intake and compression strokes for an IVO advance of 40 CAD. All the above explains why the benefit of VVT in indicated efficiency under these operating conditions is more limited than under throttling, as checked by comparing Fig. 6d and Fig. 8d maps. A maximum indicated efficiency improvement of 0.6% can be achieved with VVT at 1500 rpm and 6 bar BMEP.

4.2.3. *Turbocharging conditions*

Fig. 10 depicts the contour maps of pumping losses (a), in-cylinder RGF (b), heat losses (c), and (net) indicated efficiency (d) as functions of IVO advance and EVC delay at 2500 rpm and 14 bar BMEP. The throttle is fully open under these operating conditions, while the VGT vanes are partially closed. Also, for some VVT configurations, the intake manifold pressure is very close to (or even higher than) the exhaust one, so a portion of the intake fresh air may be short-circuited during the valve overlap. As stated in Section 3, the results of those simulations in which the trapping ratio is lower than 100% are excluded from Fig. 10 maps, in order to avoid comparing cases with different effective air dilutions. Moreover, the results obtained with VVT 0–0 and VVT 0–40 (marked with a cross and circle in Fig. 10d) are particularly analyzed to assess the impact of delaying EVC on indicated efficiency. Fig. 11 illustrates (a) the in-cylinder pressure-volume diagram, zooming in on the pumping loop, and (b) the cumulative heat losses throughout the engine cycle, normalized by fuel energy, for the two VVT configurations just mentioned. Fig. 11b also shows the instantaneous in-cylinder temperature.

Minimizing the valve overlap optimizes fuel consumption at this operating point. An improvement of around 2% in indicated efficiency is observed when comparing the results with the best (0–0) and worst (0–40) VVT configurations. This 2% improvement is owing to a reduction in pumping losses of 1.2% (Fig. 10a) and a decrease in heat losses of 0.8% (Fig. 10c). If simply analyzing the cycle-averaged variables, the pressure difference between the exhaust and intake manifolds is quite similar for both VVT configurations (1.86–1.75 bar vs. 1.95–1.83 bar).

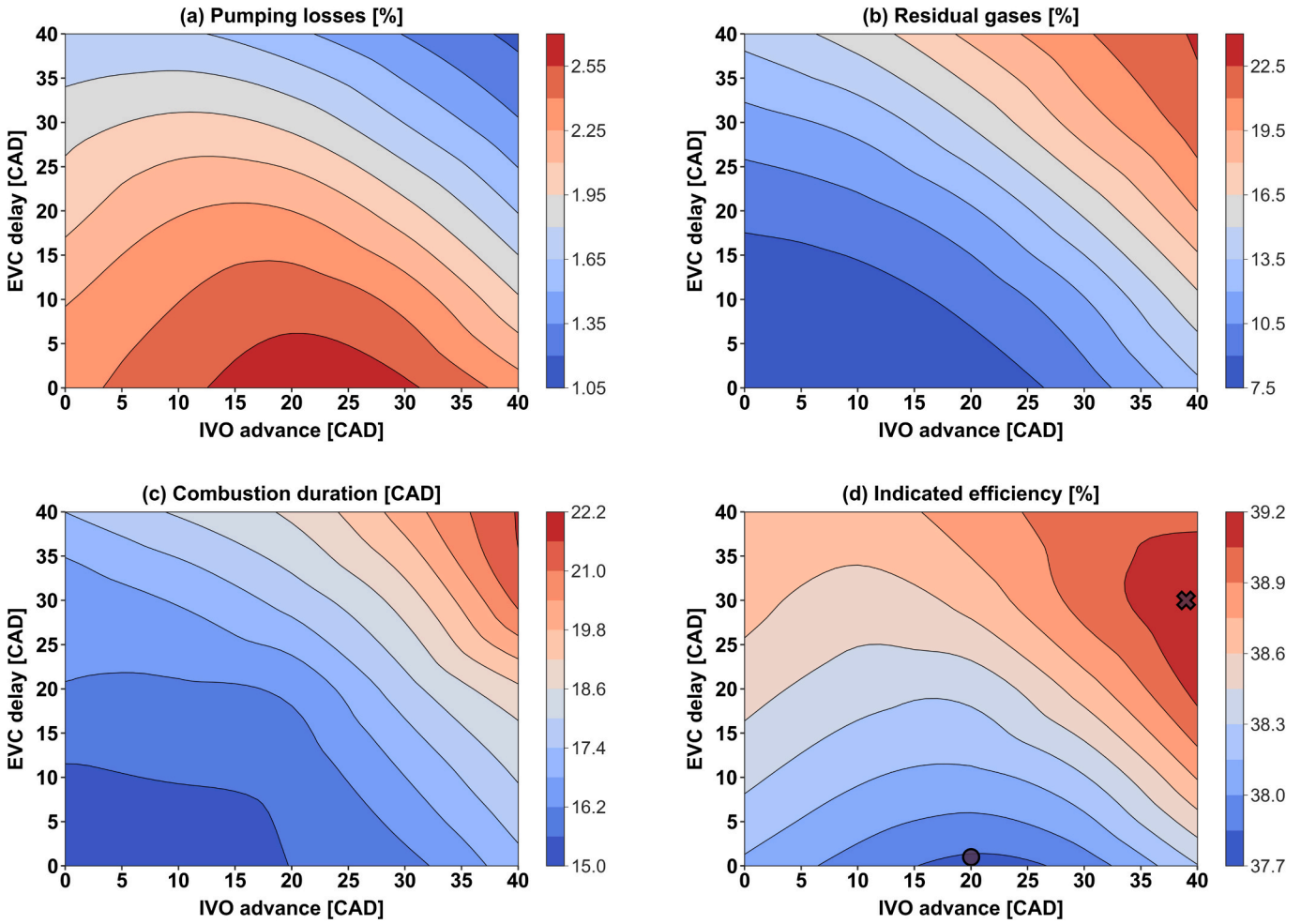

Fig. 6. Contour maps of pumping losses (a), in-cylinder RGF (b), combustion duration (c), and indicated efficiency (d) as functions of IVO advance and EVC delay at 1250 rpm and 4 bar BMEP (λ = 2).

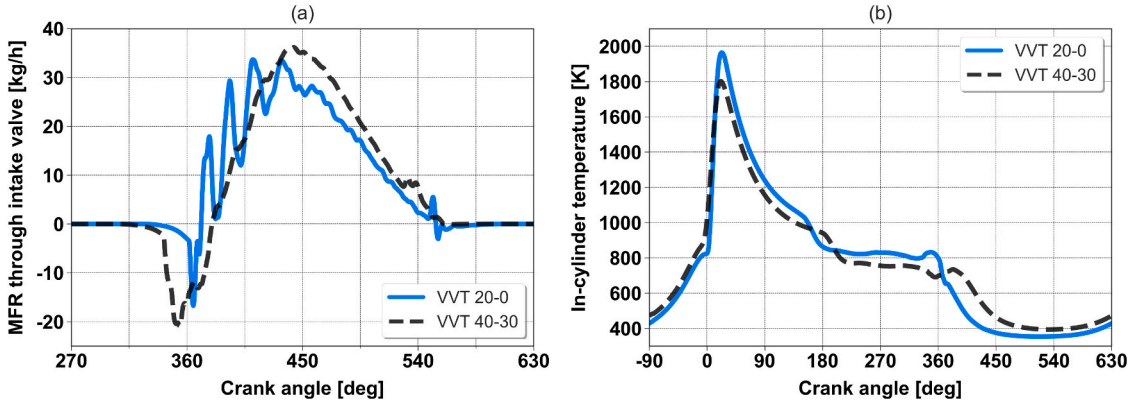

Fig. 7. Crank-angle resolved MFR through intake valves (a) and in-cylinder temperature at 1250 rpm and 4 bar BMEP (λ = 2) for the best (40–30) and worst (20−0) VVT configurations. The firing TDC is at 0 CAD.

However, Fig. 11a reveals that the in-cylinder pressure is substantially higher during most of the exhaust stroke when delaying EVC (and, consequently, the exhaust valve opening) by 40 CAD. In fact, the work done by the engine to expel burnt gases from the cylinders is 45% greater with VVT 0–40 than with VVT 0–0, justifying the difference of 1.2% in pumping losses. Regarding heat losses, delaying EVC also means a higher in-cylinder temperature during the exhaust stroke, increasing heat transfer through the cylinder walls. Fig. 11b shows that heat losses in the simulations with VVT 0–0 and VVT 0–40 only differ once the exhaust valves are opened in the first one (around 150 CAD). Between both cases, there is barely any difference in the in-cylinder gas composition and combustion process.

4.2.4. *Overview of the VVT impact*

Table 4 shows the best IVO and EVC settings in terms of thermal efficiency for the 16 steady-state operating conditions selected for this

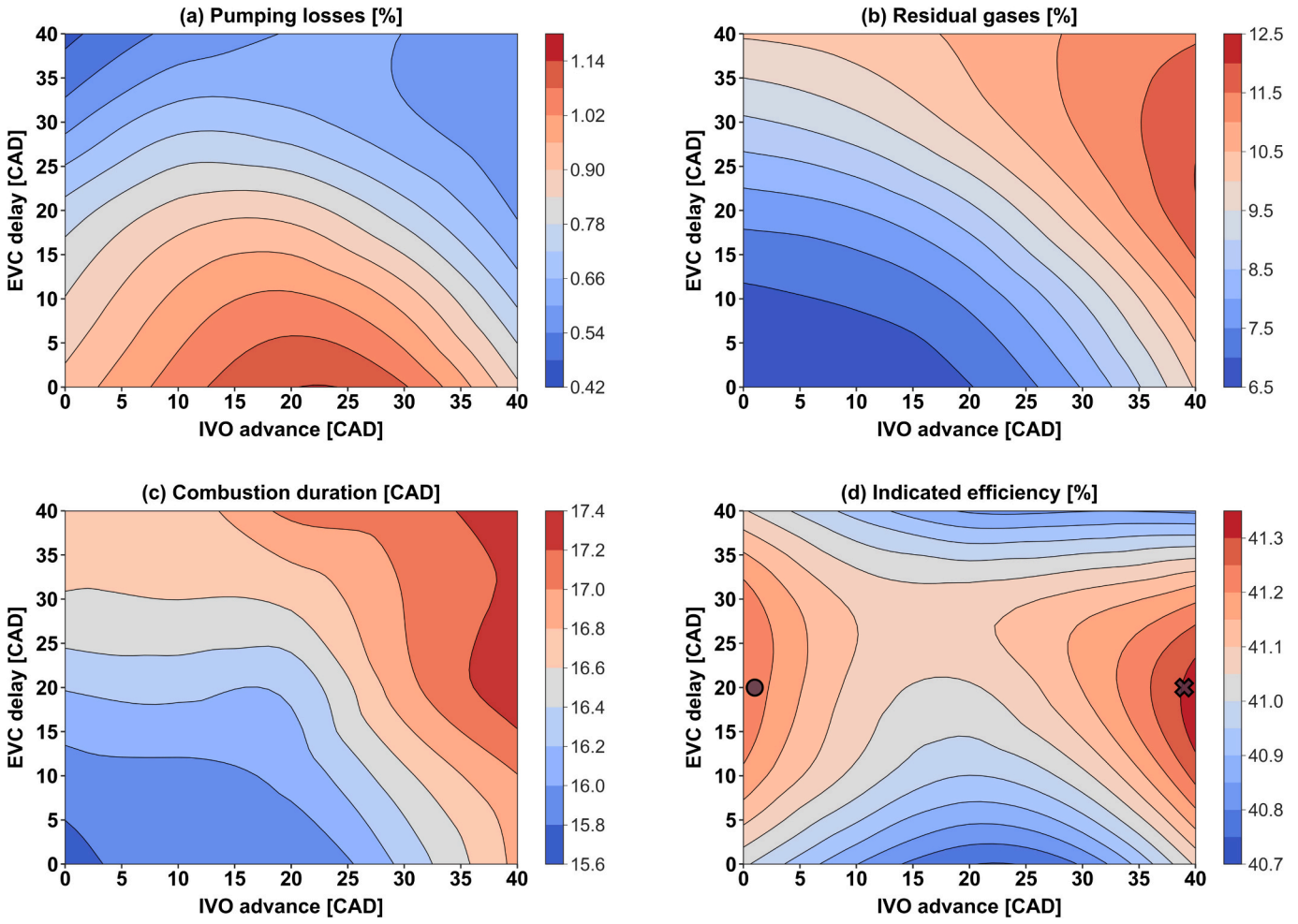

Fig. 8. Contour maps of pumping losses (a), in-cylinder RGF (b), combustion duration (c), and indicated efficiency (d) as functions of IVO advance and EVC delay at 1500 rpm and 6 bar BMEP ($\lambda = 2$).

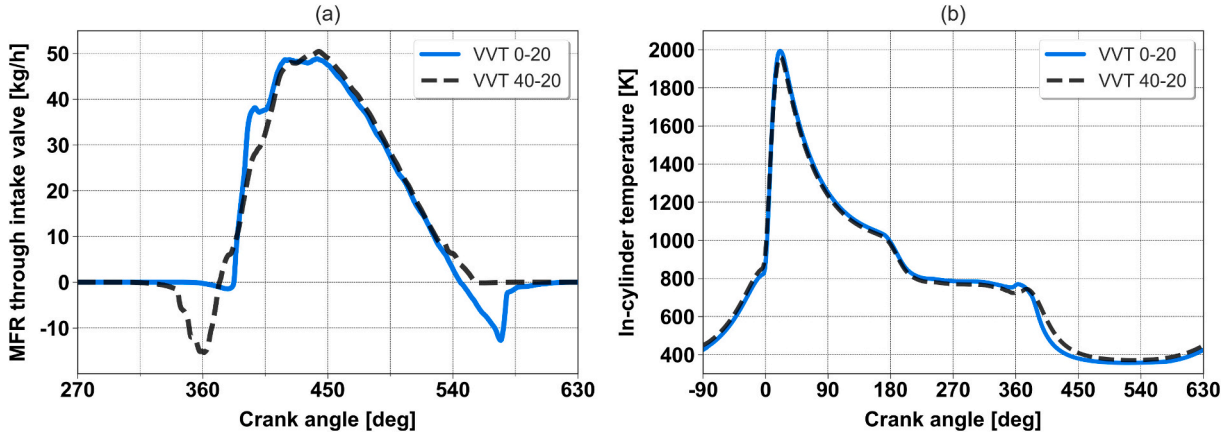

Fig. 9. Crank-angle resolved MFR through intake valves (a) and in-cylinder temperature at 1500 rpm and 6 bar BMEP ($\lambda = 2$) for the VVT 0–20 and 40–20 configurations. The firing TDC is at 0 CAD.

research. Table 4 also includes the type of condition, based on the degree of load (or how the engine load is controlled); the values of intake manifold pressure (p_{int}) and indicated efficiency (η_{ind}) obtained through the best VVT configuration; and the VVT potential to improve fuel consumption, defined as the difference between the maximum and minimum values of η_{ind} at each working point. Furthermore, Fig. A1 and Fig. A2 in the Appendix A depict the contour maps of indicated efficiency as functions of IVO advance and EVC delay for all operating conditions, not including those already shown in previous sections. Considering all these results, the following findings were identified regarding the influence of VVT on indicated efficiency:

- With the engine operating under throttling conditions with $\lambda = 2$, pumping losses are minimized through the maximum valve overlap.

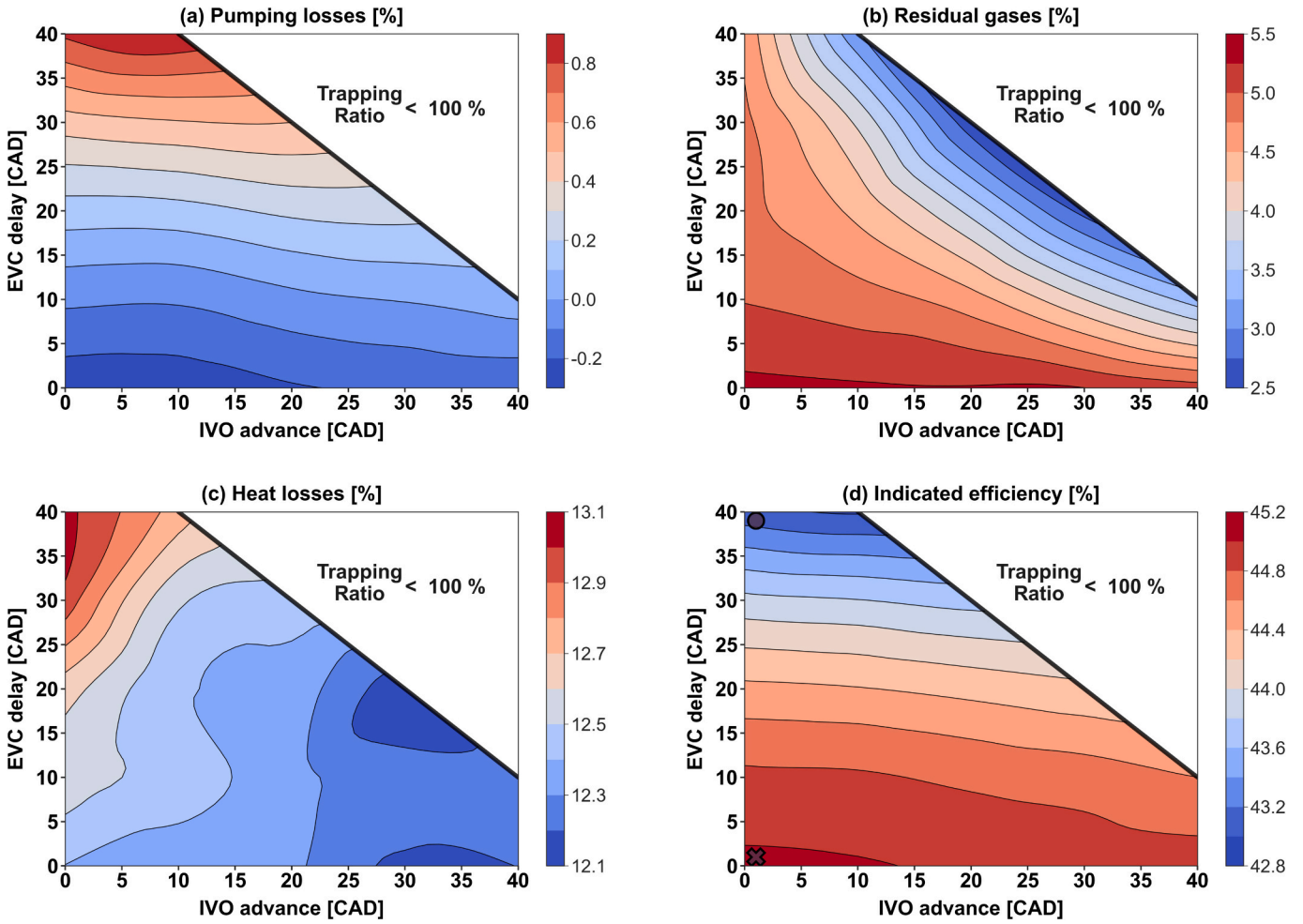

Fig. 10. Contour maps of pumping losses (a), in-cylinder RGF (b), heat losses (c), and indicated efficiency (d) as functions of IVO advance and EVC delay at 2500 rpm and 14 bar BMEP ($\lambda = 2$).

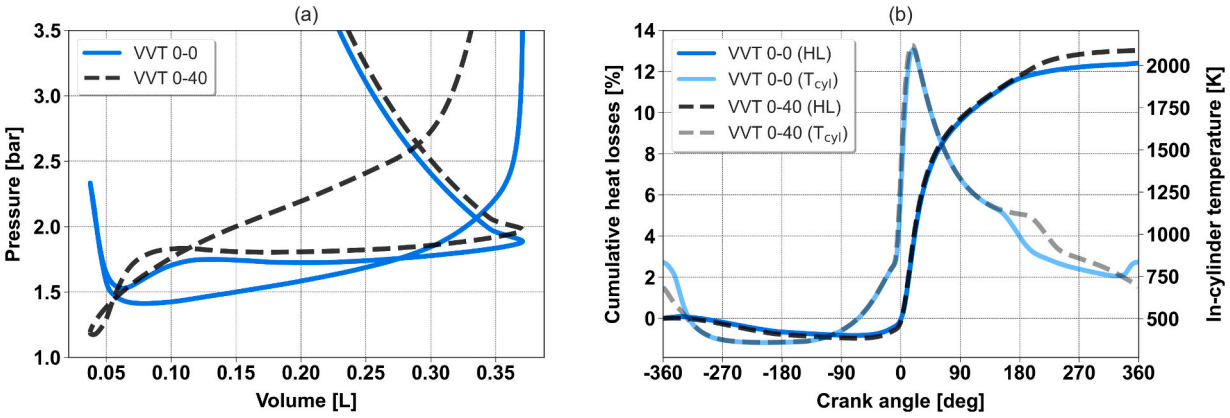

Fig. 11. In-cylinder pressure-volume diagram (a) and cumulative heat losses throughout the engine cycle (b) at 2500 rpm and 14 bar BMEP ($\lambda = 2$) for the VVT 0–0 and 0–40 configurations. The second plot also shows the instantaneous in-cylinder temperature.

However, increasing the overlap period is limited by the combustion deterioration caused by an excessive amount of residual gases. This effect explains why indicated efficiency is optimized using a long, but not the maximum, valve overlap at low loads. Optimizing the VVT system under these operating conditions can reduce fuel consumption by up to 1.5%.

- With the engine operating under turbocharged conditions, fuel consumption is optimized using VVT configurations that provide overlap periods close to the minimum. Mainly because of the impact of exhaust valve timing on pumping losses, given that an early exhaust valve opening facilitates removing burnt gases from the cylinders, resulting in decreased pumping work. In comparison, the effect of varying IVO is generally minimal. The VVT strategy under these conditions (medium and high loads) can improve fuel efficiency by 1.2–2.5%.

Table 4
Best IVO and EVC settings in terms of thermal efficiency for all steady-state operating points researched.

Speed (rpm)	BMEP (bar)	Load condition	Best IVO advance (CAD)	Best EVC delay (CAD)	p_{int} (bar)	η_{ind} (%)	$\Delta\eta_{ind}$ (%)
1250	4	Throttling	40	30	0.88	39.1	1.5
1250	12	Turbocharging	10	5	1.58	43.6	1.9
1500	2	Throttling	40	15	0.59	35.1	1.3
1500	6	Open throttle	40	20	0.99	41.3	0.6
1500	12	Turbocharging	10	5	1.58	44.3	1.2
1500	20	Turbocharging	15	0	2.67	45.3	2.0
2000	2	Throttling	40	20	0.61	35.9	1.3
2000	6	Open throttle	40	15	0.97	42.2	0.7
2000	10	Turbocharging	10	5	1.33	44.3	1.4
2000	15	Turbocharging	0	0	1.99	45.4	1.8
2000	24	Turbocharging	5	0	2.97	46.2	2.0
2500	3	Throttling	40	20	0.68	38.4	0.7
2500	6	Open throttle	0	5	0.95	42.4	1.2
2500	14	Turbocharging	0	0	1.86	45.0	2.0
3000	12	Turbocharging	10	0	1.62	44.5	2.4
3000	21	Turbocharging	0	0	2.88	45.0	2.5

- When operating in the transition zone from throttling to turbocharging, the difference between increasing and decreasing the valve overlap is lower in terms of efficiency. In other words, the potential for improvement through the VVT system is more limited. At these intermediate conditions, the indicated efficiency is maximized using long valve overlaps (as under throttling) until 2000 rpm and short ones (as under turbocharging) from 2500 rpm (Table 4).

4.3. EGR influence

4.3.1. Iso-dilution conditions

Twenty-four hydrogen engine simulations with EGR were done under iso-dilution conditions, meaning that an external dilution rate of 100% was maintained by proportionally substituting fresh air with EGR gases (see Section 3). In particular, the EGR rate was varied from 0 to 25% in increments of 5% for the following four operating points: 1250 rpm and 4 bar BMEP (low engine load), 1500 rpm and 6 bar BMEP (medium-low), 2500 rpm and 14 bar BMEP (medium-high), and 2000 rpm and 24 bar BMEP (high). The VVT settings optimized with $\lambda = 2$ and no EGR for each operating point (Table 4) were used in these simulations. Fig. 12 illustrates the indicated efficiency (a) and brake-specific NO_X emissions (b) for different EGR rates under iso-dilution conditions. Similarly, Fig. 13 shows heat losses (a), maximum in-cylinder temperature (b), combustion duration (c), and exhaust port temperature (d). Among the twenty-four simulations with EGR, the ones in which hydrogen combustion was very deteriorated (CA1090 higher than 40 CAD) were excluded from both figures. This threshold is based on the direct relationship between combustion duration (CA1090) and cycle-to-cycle variability. Observations from experiments used to calibrate and validate the combustion model indicated that cyclic variability significantly increases beyond 40 CAD of combustion duration [15]. This procedure ensures that the conclusions drawn from the simulation results are sufficiently reliable and robust.

Fig. 12 reveals that both indicated efficiency and NO_X emissions are reduced as the EGR rate increases, independently of the operating point. The penalty in efficiency is basically attributed to a slower combustion process when EGR is used. This slower H_2 combustion is responsible for a slight decrease in pumping losses under turbocharged conditions, thanks to slightly higher exhaust port temperatures, and for reduced heat losses due to lower combustion temperatures (see Fig. 13). However, these favorable effects are insufficient to offset the combustion deterioration, resulting in worse thermal efficiency. Regarding NO_X emissions, substituting fresh air for EGR gases reduces the O_2 concentration in the combustion chamber, which, along with lower combustion temperatures, explains why NO_X emissions are lower as the EGR rate increases. Finally, it should be remarked that EGR rates of around 10% could be considered valuable, particularly at medium and high loads, given that a NO_X emission reduction of 30% would be achieved with a minimal effect on fuel efficiency.

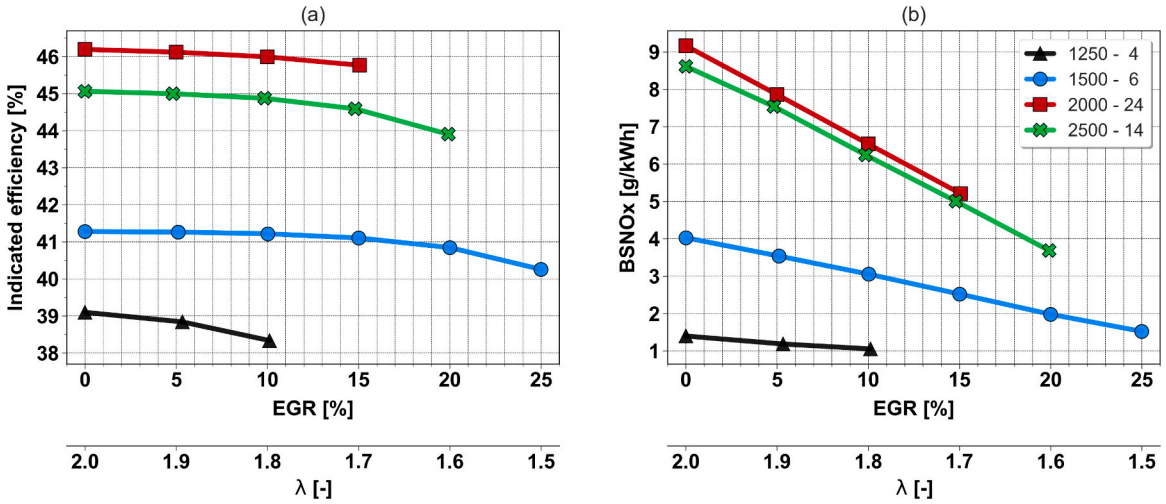

Fig. 12. Indicated efficiency (a) and brake-specific NO_X emissions (b) for different EGR rates under iso-dilution conditions. In the legend, the first value is engine speed (rpm), and the second is engine BMEP (bar).

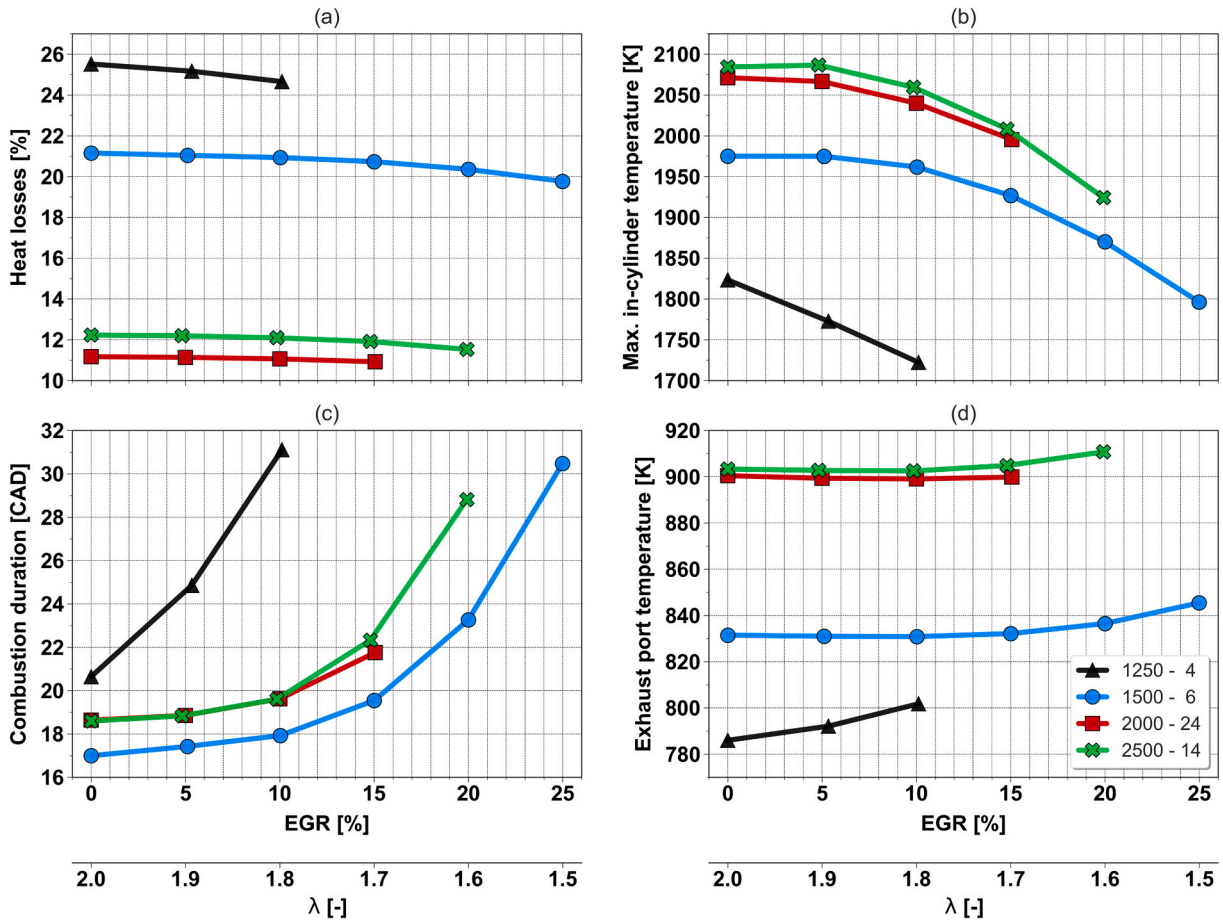

Fig. 13. Heat losses (a), maximum in-cylinder temperature (b), combustion duration (c), and exhaust port temperature (d) for different EGR rates under iso-dilution conditions. In the legend, the first value is engine speed (rpm), and the second is engine BMEP (bar).

4.3.2. *Iso-NO_X conditions*

The modeling results in Fig. 12 have demonstrated that EGR gases are more effective than fresh air in minimizing NO_X emissions. In other words, the dilution rate (air + EGR) required for a specific NO_X level is lower as the EGR rate becomes higher. A lower DR for the same boost pressure involves introducing more fuel, thus increasing engine load.

A series of hydrogen engine simulations were conducted to determine how much the peak torque can be improved using EGR without increasing NO_X emissions at 1250 and 1500 rpm, where the turbocharger is the limiting factor. In these simulations, the EGR rate was adjusted for different λ values (< 2) to obtain the same mass flow rate of NO_X as with no EGR (and $\lambda = 2$) at full load, provided that a low knocking risk was guaranteed. Fig. 14 depicts the VGT opening (a), λ (b), dilution rate (c), and fuel consumption increase (d) for different EGR rates at full load under iso-NO_X conditions. Likewise, Fig. 15 illustrates the torque increase (a), indicated efficiency (b), boost pressure increase (c), and turbine inlet temperature (d). The increases in fuel consumption, torque, and boost pressure were calculated relative to their initial values for 0% EGR ($\lambda = 2$).

As expected, regardless of engine speed, a lower dilution rate was required as the EGR rate was increased in order not to exceed a given NO_X emission level, explaining why a higher amount of fuel could be introduced. Focusing on the cases at 1250 rpm, in which VGT vanes are fully closed (**Fig. 14**a), burning additional fuel with a reduced DR leads to a boost pressure increase due to a higher turbine inlet temperature (**Fig. 15**c and d). Therefore, even more fuel can be injected. At 1500 rpm, by contrast, a similar change in the turbine inlet conditions does not translate to a boost pressure increase, given that engine power is limited by compressor surge rather than turbine performance. This justifies why there is more margin to increase engine torque at 1250 rpm than at 1500 rpm. For both speeds, the torque reaches its maximum value once the additional fuel does not compensate for the decrease in thermal efficiency (resulting from slower combustion with EGR). In short, thanks to the EGR strategy, the peak torque could be improved by 5 and 16% at 1500 and 1250 rpm, respectively, without increasing NO_X emissions. Nevertheless, it should be noted that the benefit of EGR can be limited by condensation issues, which may appear with EGR rates above 25%, given the intake flow conditions at the compressor inlet.

5. Summary and conclusions

The impact of combined VVT and EGR strategies on the performance and emissions of a Euro 6 turbocharged DI SI engine fueled with hydrogen was analyzed. To this end, a 1D model of the whole SI engine, previously validated using gasoline-fueled engine tests, was adapted for hydrogen operation. This adaptation consisted of hardware modification and a predictive hydrogen combustion submodel. Regarding the former, the turbocharger was scaled down by 20% and the exhaust manifold was thermally insulated, both to avoid a power loss using hydrogen as a fuel with λ equal to 2, respecting the original engine performance with gasoline.

Once the 1D model was adapted, hydrogen engine simulations were performed to optimize VVT settings for thermal efficiency with no EGR and λ equal to 2. The results from these simulations revealed that fuel efficiency was optimized by configuring the VVT system to provide long valve overlaps under throttling conditions (low loads) and short ones under turbocharged conditions (medium and high loads), independently of engine speed. In the transition zone from throttling to turbocharging,

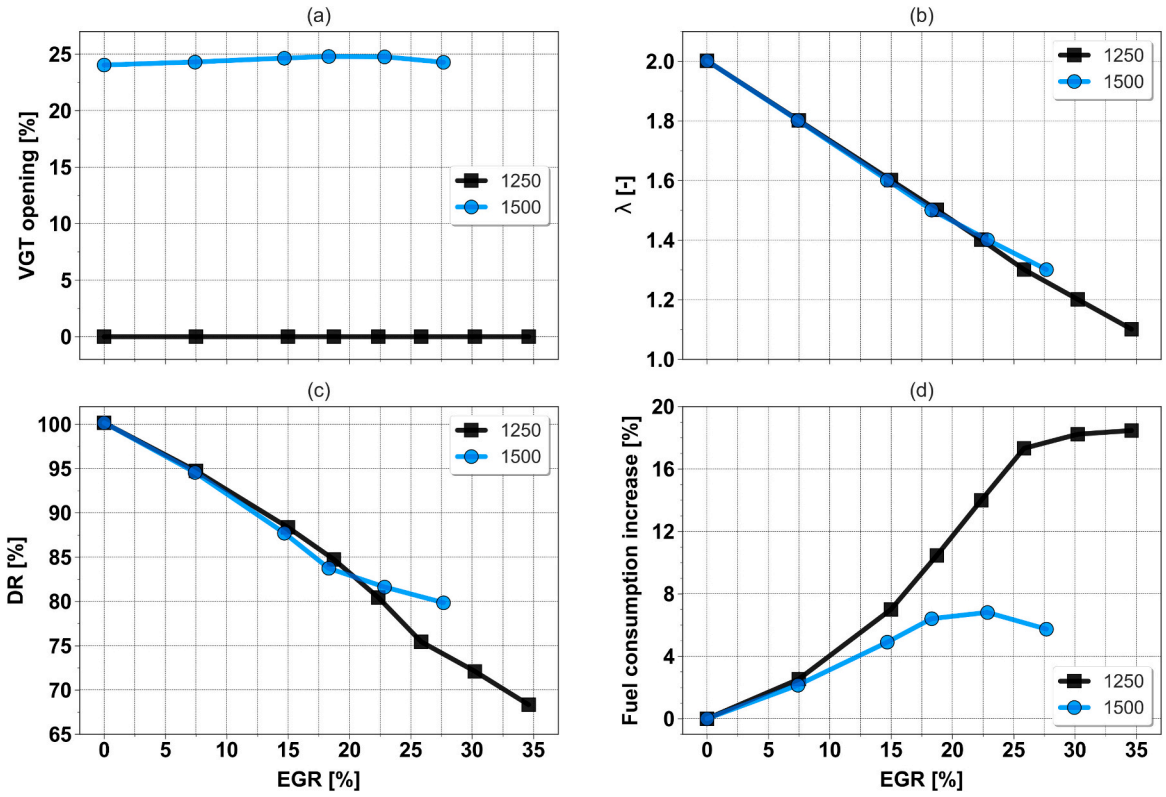

Fig. 14. VGT opening (a), λ value (b), dilution rate (c), and fuel consumption increase (d) for different EGR rates at full load under iso-NO_X conditions. In the legend, the number refers to engine speed (rpm).

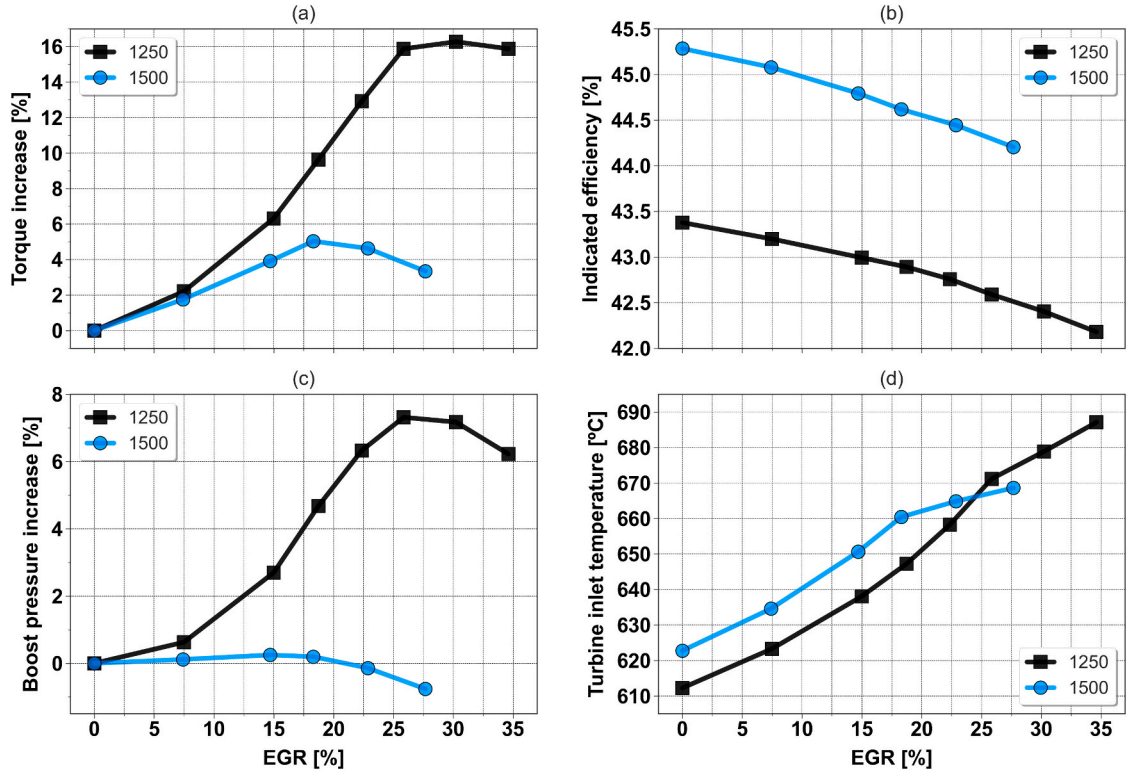

Fig. 15. Torque increase (a), indicated efficiency (b), boost pressure increase (c), and turbine inlet temperature (d) for different EGR rates at full load under iso-NO_X conditions. In the legend, the number is engine speed (rpm).

fuel efficiency was maximized using long valve overlaps (as under throttling) until 2000 rpm and short ones (as under turbocharging) from 2500 rpm. All of this could be explained by the influence of VVT on pumping losses, in-cylinder gas composition, and combustion performance. Besides, it was found that the potential of VVT for improvement is generally higher at medium and high engine loads, where thermal efficiency could be increased by up to 2.5%.

Later, EGR sweeps were simulated under iso-dilution conditions at four operating points related to different engine load levels (low, medium-low, medium-high, and high), using the VVT settings optimized before without EGR. These simulations revealed that diluting with EGR gases rather than fresh air is more effective in reducing NO_X due to lower in-cylinder O_2 concentrations and combustion temperatures; however, EGR slightly penalizes fuel economy. More specifically, EGR rates of 10%, while maintaining an external dilution rate of 100%, were found to decrease NOx emissions by 30% at medium and high loads with minimal impact on thermal efficiency. Finally, two additional EGR sweeps were simulated at full load but now under iso-NO_X conditions. These last simulations showed that EGR leads to higher low-end torque due to the lower total dilution rate required for a given NO_X level (given that EGR is more effective in minimizing NO_X). In particular, the EGR strategy would improve peak torque by 5 and 16% at 1500 and 1250 rpm, respectively, without affecting NO_X emissions.

CRediT authorship contribution statement

Ricardo Novella: Supervision, Resources, Project administration, Conceptualization. **Josep Gomez-Soriano:** Writing – review & editing, Writing – original draft, Supervision, Methodology, Formal analysis, Conceptualization. **David González-Domínguez:** Writing – review & editing, Writing – original draft, Visualization, Methodology, Formal analysis, Conceptualization. **Orlando Olaciregui:** Writing – review & editing, Visualization.

Declaration of competing interest

The authors declare that they have no known competing financial interests or personal relationships that could have appeared to influence the work reported in this paper.

Data availability

Data will be made available on request.

Acknowledgements

Funding for open access charge: CRUE-Universitat Politècnica de València.

Appendix A

Fig. A1 shows the contour maps of indicated efficiency as functions of IVO advance and EVC delay for the next operating points: 1250 rpm and 12 bar BMEP (a), 1500 rpm and 2 bar BMEP (b), 1500 rpm and 12 bar BMEP (c), 1500 rpm and 20 bar BMEP (d), 2000 rpm and 2 bar BMEP (e), and 2000 rpm and 6 bar BMEP (f). The results of the simulations in which the trapping ratio is lower than 100% are not shown. Those simulations at low engine loads in which the combustion is very deteriorated for long overlap periods are neither considered. Likewise, Fig. A2 illustrates the contour maps of indicated efficiency for the following operating points: 2000 rpm and 10 bar BMEP (a), 2000 rpm and 15 bar BMEP (b), 2000 rpm and 24 bar BMEP (c), 2500 rpm and 3 bar BMEP (d), 2500 rpm and 6 bar BMEP (e), 3000 rpm and 12 bar BMEP (f), and 3000 rpm and 21 bar BMEP (g).

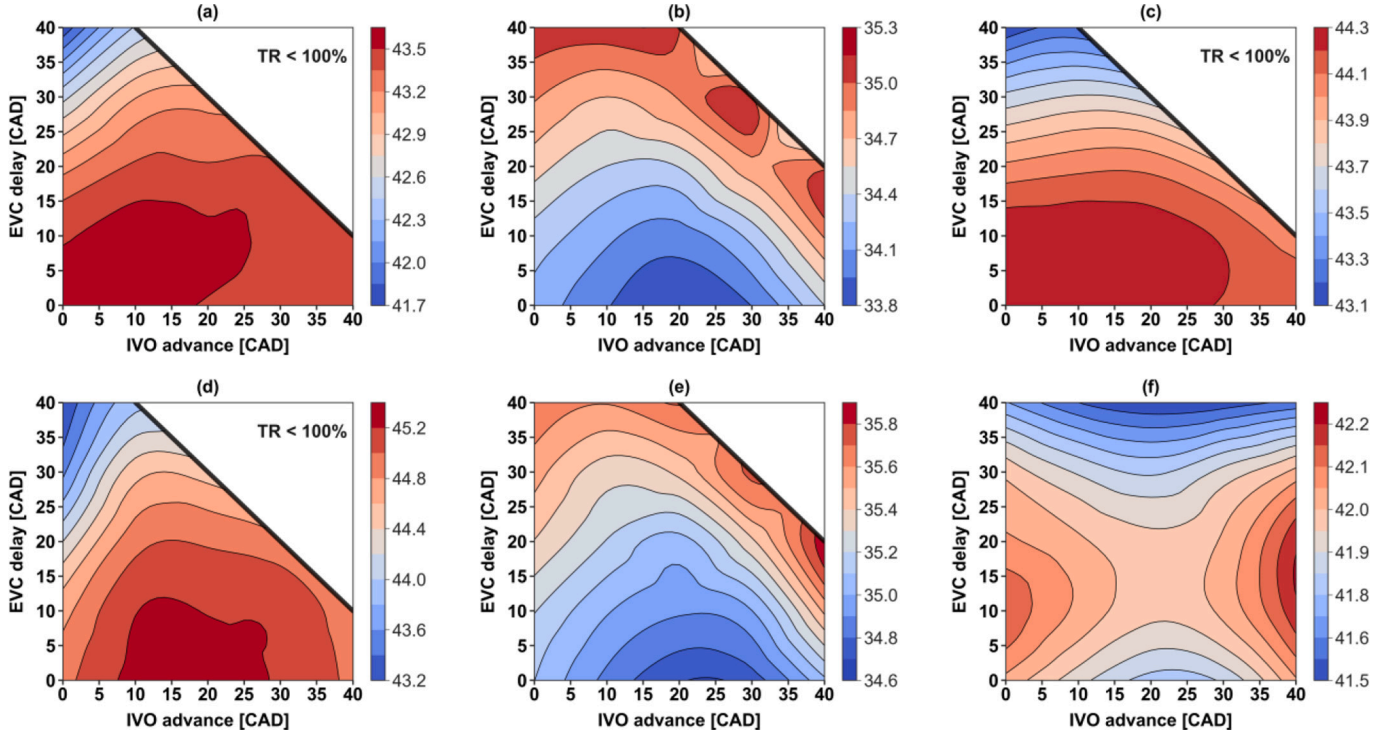

Fig. A1. Contour maps of indicated efficiency, as functions of IVO advance and EVC delay, with $\lambda = 2$ for the next operating points: 1250 rpm and 12 bar BMEP (a), 1500 rpm and 2 bar BMEP (b), 1500 rpm and 12 bar BMEP (c), 1500 rpm and 20 bar BMEP (d), 2000 rpm and 2 bar BMEP (e), and 2000 rpm and 6 bar BMEP (f).

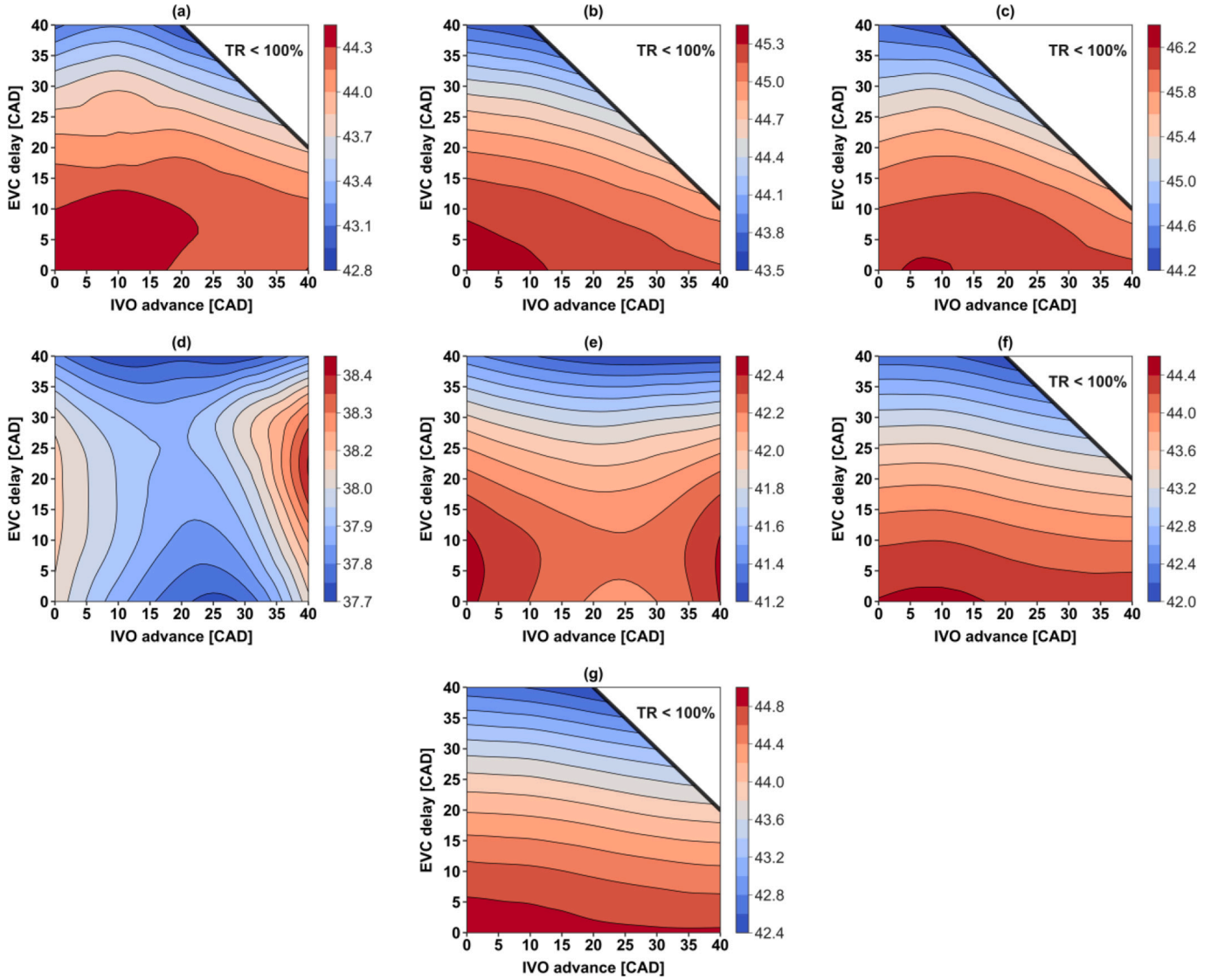

Fig. A2. Contour maps of indicated efficiency, as functions of IVO advance and EVC delay, with $\lambda = 2$ for the next operating points: 2000 rpm and 10 bar BMEP (a), 2000 rpm and 15 bar BMEP (b), 2000 rpm and 24 bar BMEP (c), 2500 rpm and 3 bar BMEP (d), 2500 rpm and 6 bar BMEP (e), 3000 rpm and 12 bar BMEP (f), and 3000 rpm and 21 bar BMEP (g).

References

[1] Ritchie H, Roser M, Rosado P. CO2 and greenhouse gas emissions: By sector. Our World in Data, https://ourworldindata.org/emissions-by-sector; 2020.

[2] Statista. Emissions in the European Union. https://www.statista.com/study/56124/emissions-in-the-european-union/.

[3] Joshi A. Review of Vehicle Engine Efficiency and Emissions. SAE Technical Paper 2021-01-0575 **2021**. https://doi.org/10.4271/2021-01-0575.

[4] U.S. Environmental Protection Agency (EPA). Revised 2023 and Later Model Year Light-Duty Vehicle Greenhouse Gas Emissions Standards. https://www.epa.gov/regulations-emissions-vehicles-and-engines/final-rule-revise-existing-national-ghg-emissions.

[5] European Parliament. Fit for 55: MEPs back objective of zero emissions for cars and vans in 2035. https://www.europarl.europa.eu/news/en/press-room/20220603IPR32129/fit-for-55-meps-back-objective-of-zero-emissions-for-cars-and-vans-in-2035; 2022.

[6] Duan YH, Sun BG, Li Q, Wu XS, Hu TG, Luo QH. Combustion characteristics of a turbocharged direct-injection hydrogen engine. Energy Convers Manag 2023;291:117267. https://doi.org/10.1016/j.enconman.2023.117267.

[7] Li J, Zhang R, Pan J, Wei H, Shu G, Chen L. Ammonia and hydrogen blending effects on combustion stabilities in optical SI engines. Energy Convers Manag 2023;280:116827. https://doi.org/10.1016/j.enconman.2023.116827.

[8] Verhelst S, Demuynck J, Martin S, Vermeir M, Sierens R. Investigation of Supercharging Strategies for PFI Hydrogen Engines. SAE Technical Paper 2010-01-0582 **2010**. https://doi.org/10.4271/2010-01-0582.

[9] Sun BG, Luo QH, Li Q, Wu X, Hu T, Bao LZ, et al. Performance optimization design of direct injection turbocharged hydrogen internal combustion engine. Appl Energy Combustion Sci 2023;16:100204. https://doi.org/10.1016/j.jaecs.2023.100204.

[10] Welch A, Mumford D, Munshi S, Holbery J, Boyer B, Younkins M, et al. Challenges in Developing Hydrogen Direct Injection Technology for Internal Combustion Engines. SAE Technical Paper 2008-01-2379 **2008**. https://doi.org/10.4271/2008-01-2379.

[11] Sierens R, Demuynck J, Vancoillie J, Sileghem L, Verhelst S. In: Efficiency comparison of hydrogen fuelled IC engines with gasoline and methanol fuelled engines. San José, Costa Rica; 2011.

[12] Verhelst S, Wallner T. Hydrogen-fueled internal combustion engines. Prog Energy Combust Sci 2009;35(6):490–527. https://doi.org/10.1016/j.pecs.2009.08.001.

[13] White CM, Steeper RR, Lutz AE. The hydrogen-fueled internal combustion engine: a technical review. Int J Hydrog Energy 2006;31(10):1292–305. https://doi.org/10.1016/j.ijhydene.2005.12.001.

[14] Verhelst S, De Landtsheere J, De Smet F, Billiouw C, Trenson A, Sierens R. Effects of supercharging, EGR and variable valve timing on power and emissions of hydrogen internal combustion engines. SAE Int J Engines 2019;1(1):647–56. https://doi.org/10.4271/2008-01-1033.

[15] Novella R, García A, Gomez-Soriano J, Fogué-Robles Á. Exploring dilution potential for full load operation of medium duty hydrogen engine for the transport sector. Appl Energy 2023;349:121635. https://doi.org/10.1016/j.apenergy.2023.121635.

[16] Heywood JB. Ideal models of engine cycles. In: Internal combustion engine fundamentals. 2nd ed. New York: McGraw-Hill Education; 2018. https://www.

accessengineeringlibrary.com/content/book/9781260116106/toc-chapter/chapter5.
[17] Jin S, Deng J, Xie K, Liang X, Wang C, Ding W, et al. Knock control in hydrogen-fueled argon power cycle engine with higher compression ratio by water port injection. Appl Energy 2023;349:121664. https://doi.org/10.1016/j.apenergy.2023.121664.
[18] Oh S, Kim C, Lee Y, Yoon S, Lee J, Kim J. Experimental investigation of the hydrogen-rich offgas spark ignition engine under the various compression ratios. Energy Convers Manag 2019;201:112136. https://doi.org/10.1016/j.enconman.2019.112136.
[19] Verhelst S, Turner JWG. Hydrogen-Fueled Spark Ignition Engines. In: Hydrogen for future thermal engines. Cham: Springer; 2023. https://doi.org/10.1007/978-3-031-28412-0_8.
[20] Dhyani V, Subramanian KA. Fundamental characterization of backfire in a hydrogen fuelled spark ignition engine using CFD and experiments. Int J Hydrog Energy 2019;44(60):32254–70. https://doi.org/10.1016/j.ijhydene.2019.10.077.
[21] Liu XH, Liu FS, Zhou L, Sun BG, Schock HJ. Backfire prediction in a manifold injection hydrogen internal combustion engine. Int J Hydrog Energy 2018;33(14):3847–55. https://doi.org/10.1016/j.ijhydene.2008.04.051.
[22] Onorati A, Payri R, Vaglieco BM, Agarwal AK, Bae C, Bruneaux G, et al. The role of hydrogen for future internal combustion engines. Int J Engine Res 2022;23(4):529–40. https://doi.org/10.1177/14680874221081947.
[23] Rasul MG, Hazrat MA, Sattar MA, Jahirul MI, Shearer MJ. The future of hydrogen: challenges on production, storage and applications. Energy Convers Manag 2022;272:116326. https://doi.org/10.1016/j.enconman.2022.116326.
[24] Climent H, Dolz V, Pla B, González-Domínguez D. Analysis on the potential of EGR strategy to reduce fuel consumption in hybrid powertrains based on advanced gasoline engines under simulated driving cycle conditions. Energy Convers Manag 2022;266:115830. https://doi.org/10.1016/j.enconman.2022.115830.
[25] Serrano JR, Arnau FJ, García-Cuevas LM, Gómez-Vilanova A, Guilain S, Batard S. A methodology for measuring turbocharger adiabatic maps in a gas-stand and its usage for calibrating control oriented and one-dimensional models at early ICE design stages. J Energy Resour Technol 2021;143(4):042303. https://doi.org/10.1115/1.4048229.
[26] Galindo J, Climent H, De la Morena J, González-Domínguez D, Guilain S. Assessment of air management strategies to improve the transient response of advanced gasoline engines operating under high EGR conditions. Energy 2023;262:125586. https://doi.org/10.1016/j.energy.2022.125586.
[27] Serrano J, Climent H, Navarro R, González-Domínguez D. Methodology to Standardize and Improve the Calibration Process of a 1D Model of a GTDI Engine. SAE Technical Paper 2020-01-1008 **2020**. https://doi.org/10.4271/2020-01-1008.
[28] Ghojel JI. Review of the development and applications of the Wiebe function: a tribute to the contribution of Ivan Wiebe to engine research. Int J Engine Res 2010;11(4):297–312. https://doi.org/10.1243/14680874JER06510.
[29] Lavoie GA, Ortiz-Soto E, Babajimopoulos A, Martz JB, Assanis DN. Thermodynamic sweet spot for high-efficiency, dilute, boosted gasoline engines. Int J Engine Res 2013;14(3):260–78. https://doi.org/10.1177/1468087412455372.
[30] Choi CR, Huh KY. Development of a coherent flamelet model for a spark-ignited turbulent premixed flame in a closed vessel. Combust Flame 1998;114(3–4):336–48. https://doi.org/10.1016/S0010-2180(97)00194-6.
[31] Jurić F, Stipić M, Samec N, Hriberšek M, Honus S, Vujanović M. Numerical investigation of multiphase reactive processes using flamelet generated manifold approach and extended coherent flame combustion model. Energy Convers Manag 2021;240:114261. https://doi.org/10.1016/j.enconman.2021.114261.
[32] Lafossas F, Colin O, Le Berr F, Menegazzi P. Application of a New 1D Combustion Model to Gasoline Transient Engine Operation. SAE Technical Paper 2005-01-2107 **2005**. https://doi.org/10.4271/2005-01-2107.
[33] Kéromnès A, Metcalfe WK, Heufer KA, Donohoe N, Das AK, Sung CJ, et al. An experimental and detailed chemical kinetic modeling study of hydrogen and syngas mixture oxidation at elevated pressures. Combust Flame 2013;160(6):995–1011. https://doi.org/10.1016/j.combustflame.2013.01.001.
[34] Karvountzis-Kontakiotis A, Ntziachristos L. Improvement of NO and CO predictions for a homogeneous combustion SI engine using a novel emissions model. Appl Energy 2016;162:172–82. https://doi.org/10.1016/j.apenergy.2015.10.088.
[35] Kherdekar PV, Bhatia D. Simulation of a spark ignited hydrogen engine for minimization of NOx emissions. Int J Hydrog Energy 2017;42(7):4579–96. https://doi.org/10.1016/j.ijhydene.2016.10.074.
[36] Douaud A, Eyzat P. Four-octane-number method for predicting the anti-Knock behavior of fuels and engines. SAE Technical Paper 1978:780080. https://doi.org/10.4271/780080.
[37] Hong C, Ji C, Wang S, Xin G, Qiang Y, Yang J. Progressive strategies to avoid and exploit knock limit for optimal performance and stoichiometric operation of a DI hydrogen engine with high CR at WOT conditions. Fuel 2024;357:129849. https://doi.org/10.1016/j.fuel.2023.129849.
[38] Özyalcin C, Sterlepper S, Roiser S, Eichlseder H, Pischinger S. Exhaust gas aftertreatment to minimize NO_X emissions from hydrogen-fueled internal combustion engines. Appl Energy 2024;353:122045. https://doi.org/10.1016/j.apenergy.2023.122045.
[39] Sterlepper S, Fischer M, Claßen J, Huth V, Pischinger S. Concepts for hydrogen internal combustion engines and their implications on the exhaust gas aftertreatment system. Energies 2021;14(23):8166. https://doi.org/10.3390/en14238166.
[40] Verhelst S, Maesschalck P, Rombaut N, Sierens R. Increasing the power output of hydrogen internal combustion engines by means of supercharging and exhaust gas recirculation. Int J Hydrog Energy 2009;34(10):4406–12. https://doi.org/10.1016/j.ijhydene.2009.03.037.